

# The development, design and characterisation of a scale model Horizontal Axis Tidal Turbine for Dynamic Load Quantification.

Matthew Allmark<sup>a,\*</sup>, Robert Ellis<sup>a</sup>, Catherine Lloyd<sup>a</sup>, Stephanie Ordonez-Sanchez<sup>b</sup>, Kate Johannesen<sup>b</sup>, Carl Byrne<sup>a</sup>, Cameron Johnstone<sup>b</sup>, Tim O'Doherty<sup>a</sup>, Allan Mason-Jones<sup>a</sup>

<sup>a</sup>Cardiff University School of Engineering, Cardiff, CF24 3AA United Kingdom

<sup>b</sup>Department of Mechanical and Aerospace Engineering University of Strathclyde, James Weir Building, Level 8, 75 Montrose Street, Glasgow, G1 1XJ

---

## Abstract

The paper describes the development and characterisation of three 0.9 m diameter lab-scale Horizontal Axis Tidal Turbines. The blade development process has been outlined and was used to generate a design specification. Each turbine houses instrumentation to measure rotor thrust, torque and blade root bending moments on each blade, in both 'flapwise' and 'edgewise' directions. A permanent magnet synchronous machine and encoder are integrated to allow for servo-control of the turbine as well as to provide position and rotational velocity measurements, resulting in three turbines that can be individually controlled using speed or torque control. Analogue signals

---

\*Corresponding author

*Email addresses:* AllmarkMJ1@cardiff.ac.uk (Matthew Allmark), EllisR10@cardiff.ac.uk (Robert Ellis), LloydC11@cf.ac.uk (Catherine Lloyd), s.ordonez@strath.ac.uk (Stephanie Ordonez-Sanchez), kate.porter.10@alumni.ucl.ac.uk (Kate Johannesen), byrne@cardiff.ac.uk (Carl Byrne), cameron.johnstone@strath.ac.uk (Cameron Johnstone), Odoherty@cardiff.ac.uk (Tim O'Doherty), mason-jonesA@cardiff.ac.uk (Allan Mason-Jones)

are captured via a real-time operating system and field programmable gate array hardware architecture facilitating sample rates of up to 2 kHz. Results from testing the pilot turbine at three differing facilities during the development process are presented. Here good agreement, less than 7% variation, was found when comparing the testing undertaken at various flume and tow tank facilities. Lastly, the findings of a test campaign to characterise the performance of each of the three turbines are presented. Very good agreement in non-dimensional values for each of the three manufactured turbines was found.

*Keywords:* Horizontal Axis Tidal Turbine, Scale Turbine Development, Computational Fluid Dynamics, ANSYS CFX, Turbine Characterisation

---

## 1. Introduction

Energy extraction from the ocean's tides has gained widespread acceptance as a potential contributor to the UK energy mix [1]. Increased interest in tidal energy extraction has, in part, been driven by the realisation of finite global resources and environmental impacts of burning fossil fuels [2]. The EU Renewable Energy Directive has recently extended previous commitments to stipulate that the EU community will fulfil 35% of its energy needs via renewable sources by 2030; it is foreseen that tidal energy extraction could go some way to helping achieve this target [3].

In order for Horizontal Axis Tidal Turbine (HATT) devices to generate energy at a competitive levelized cost of energy (LCOE), effective strategies for reducing device over-engineering and the burden of operation and maintenance costs are required. In order to achieve the 20 year lifespan [4] -

14 quoted as being required for cost effective energy extraction - whilst reducing  
15 device over engineering, detailed understanding of HATT operational loads  
16 is required. Knowledge of normal operational loads, extreme operational  
17 loads and the characteristics of load fluctuations is required to minimise the  
18 probability of device failure due to overloading and fatigue.

19 During the projected turbine life cycle, extreme loads can arise from  
20 current-wave interactions, from flow acceleration around upstream turbines  
21 and from high speed turbulent structures in the on-coming fluid flow. Fur-  
22 thermore, these loads sources, as well as the effects of tidal cycles and turbine  
23 rotation, lead to a variety of cyclic loading events at various magnitudes and  
24 frequencies. In moving towards robust and cost effective designs, understand-  
25 ing and quantification of these loads will be required. It would seem pertinent  
26 to develop a series of standard load specifications under a number of oper-  
27 ational and environmental scenarios to which turbines can be designed and  
28 ultimately 'signed-off' against - similar to the IEC 61400 standard for the  
29 wind industry [5]. Although difficulties in adapting such an approach to the  
30 tidal industry surely exist, such a methodology will allow for increased load  
31 understanding, design maturity and improved turbine life expectancy fore-  
32 casting. Developments in the above are likely to bolster investor confidence  
33 and will aid in device underwriting by insurance companies - two important  
34 aspects that need to be addressed in order to create a functioning industry  
35 for the future.

36 This paper outlines the development process undertaken in designing and  
37 manufacturing three instrumented 1/20th scale HATT devices in order to  
38 understand the dynamic loading of HATTs, to inform developers and help

39 achieve survivability and efficiencies in the marine energy sector. The three  
40 devices have been manufactured and used for testing of HATTs singularly  
41 as well as in array configurations. In this way the impacts of array opera-  
42 tion and structure on turbine loading can be studied at scale. The paper  
43 describes the design specification, testing of the three HATTs at three sepa-  
44 rate test facilities (the Consiglio Nazionale delle Ricerche Institute of Marine  
45 Engineering (CNR-INM) wave-tow tank, the Institut Francais de Recherche  
46 pour l’exploitation de la mer (IFREMER) re-circulating flume and the Kelvin  
47 Hydrodynamic Laboratory (KHL) tow tank) to characterise each turbine in-  
48 dividually against the specifications. The individual data outputs were then  
49 compared to check for consistency. Initially the results relating to a sin-  
50 gular turbine undergoing testing at the CNR-INM facility are presented, this  
51 followed by a comparison of the outputs of the three turbines recorded at  
52 KHL. Lastly, a detailed analysis of the turbine performance at the IFRE-  
53 MER flume is presented considering the repeatability of the turbine mea-  
54 surements, the dimensional power and thrust performance, the drive shaft  
55 losses and Reynolds effects associated with turbine operation under low tur-  
56 bulence intensity flow regimes.

## 57 **2. A Review of Lab-Scale Turbine Testing and Design**

58 For the last 15-20 years, testing and development of scale model tur-  
59 bines has been utilised in both research and by turbine developers [6–12].  
60 Scale model testing has allowed developers to further understand design deci-  
61 sions during early Technology Readiness Levels (TRLs) with relatively small  
62 investments needed. In terms of research, the use of scale model HATTs

63 has proliferated and allowed researchers to understand the fundamental fluid  
64 dynamics, loading mechanisms and efficiencies associated with a variety of  
65 HATT rotor configurations. Furthermore, scale model testing has formed a  
66 vital part of using numerical modelling techniques to inform design modi-  
67 fications, both economically and relatively quickly, by providing validation  
68 data. Generally, scale testing to-date has proceeded at the 1/30th or higher  
69 depending on the size of the test facilities available for testing such devices.  
70 The use of nursery sites, however, has allowed for the development and test-  
71 ing of 1/5th scale devices - which is often a crucial step in moving towards  
72 a higher TRL full-scale deployments. As the turbine development detailed  
73 within this paper is specific to a 1/20th scale HATT this review section will  
74 be constrained to consider the form case exclusively.

75 In terms of first-hand experience gained by the authors, Cardiff Marine  
76 Energy Research Group (CMERG) has previously developed three working  
77 0.5 m diameter turbines. These have been used to conduct turbine design  
78 studies using CFD. Both turbines were developed using the HATT form.  
79 Details of the first turbine arrangement can be found in [13]. Testing with  
80 the first generation turbine was successful in validating and informing CFD  
81 models developed within the research group. The second generation lab-  
82 scale HATT was also developed, details of which are outlined in [14, 15]. The  
83 turbine rotor and braking motor were directly coupled via a short drive shaft.  
84 This required that the motor was mounted inside the turbine housing, i.e. in  
85 the manner that is similar to many commercial turbine set ups with the motor  
86 taking the position of a Permanent Magnet Synchronous Machine (PMSM -  
87 typically used for direct drive applications). Thrust on the turbine structure,

88 including the stanchion was measured. This turbine was used extensively in  
89 studying the power converted and wake recovery associated with the rotor  
90 under plug flows, profiled flows, flow misalignment, wave current interaction  
91 and blade fault diagnostics [13–18]. A third generation turbine was then  
92 designed within CMERG. The turbine was created using a similar rotor setup  
93 to the previous model scale allowing for both speed and torque control of  
94 the turbine. The turbine was fitted with a thrust and twisting moment  
95 transducer for a single blade, as well as an accelerometer housed in the nose  
96 cone. The rotor data captured was logged remotely via an Arduino mounted  
97 in the turbine nose cone. A similar stanchion arrangement was used to  
98 measure thrust loading on the turbine. The torque developed via the turbine  
99 rotor was measured via the integrated PMSM. This generation HATT was  
100 used for a variety of test campaigns studying turbine rotor faults, the effect  
101 of turbine yaw angle, wave loading effects and bend-twist coupling for blade  
102 load shedding [13–19].

### 103 **3. Blade Design**

104 The blade, and ultimately the rotor, design of the detailed lab-scale device  
105 was developed to allow for adherence to Reynolds scaling and preservation  
106 of the Kinematic relationship between the blade tip speed relative to the  
107 incident fluid velocity. Details on the approach to Reynolds scaling can be  
108 found [20]. The Wortmann FX63-137 aerofoil has been used by CMERG for  
109 producing scaled HATT blades. Initially designed by Egarr [21], the blades  
110 have been extensively tested both numerically and experimentally [13], [15].  
111 The aerofoil has high lift and low stall characteristics and a large root chord

112 length which aids a self starting capability [4]. An important aspect of the  
 113 design and development of the turbine was the development of an optimised  
 114 turbine rotor based on the Wortmann FX63-137 aerofoil. The chord lengths,  
 115 twist distribution from root to tip, pitch angle and hub attachment method  
 116 were all studied, with the goal of increasing the power coefficient,  $C_P$ , from  
 117 a peak of 0.4 while maintaining the thrust coefficient,  $C_T$ , to within 10% of  
 118 the levels observed in the previous blade geometry (i.e.  $C_T \approx 0.88$  at Peak  
 119  $C_P$  and  $\approx 0.99$  at freewheeling).

120 To aid the development of the rotor and turbine specification, the non-  
 121 dimensional coefficients have been utilised and defined by Equations 1 to 4,  
 122 below. Dimensional data have, however, been used where appropriate and  
 123 specified along with a reference fluid velocity.

$$C_P(\lambda) = \frac{Power}{0.5\rho AV^3} \quad (1)$$

$$C_\theta(\lambda) = \frac{Torque}{0.5\rho ARV^2} \quad (2)$$

$$C_t(\lambda) = \frac{Thrust}{0.5\rho AV^2} \quad (3)$$

124 where the tip speed ratio ( $\lambda$ ), is given as,

$$\lambda = \frac{\omega R}{V} \quad (4)$$

125 where,  $V$  is the fluid velocity in  $ms^{-1}$ ,  $\rho$  is the density of water in  $kg/m^3$ ,  
 126  $A$  is the turbine swept area in  $m^2$ ,  $R$  is the turbine radius in  $m$  and  $\omega$  is the

127 rotational velocity in  $rads^{-1}$ . The two methods used for the design develop-  
128 ment were Blade Element Momentum Theorem (BEMT) and Computational  
129 Fluid Dynamics (CFD).

130

### 131 *3.1. Blade Element Momentum Theory*

132 Optimising the blade design based on the Wortmann FX 63-137 profile  
133 was conducted in two stages: 1) the chord length distribution from blade  
134 root to tip and 2) the blade twist distribution. In total over 130 variations  
135 were considered using the University of Strathclyde BEMT code [22]. One of  
136 the main reasons for using BEMT initially is that the execution and compila-  
137 tion of the code is comparatively simple, when compared to other numerical  
138 methods and the blade design can be produced quickly, allowing for the ef-  
139 ficient study of a large number of blade geometry cases as required. The lift  
140 and drag coefficients for the Wortmann aerofoil were calculated using XFOIL.  
141 The  $C_P$  and  $C_T$  were compared for various chord length and twist distribu-  
142 tions. Those designs with the highest performance coefficients were plotted  
143 and the peak  $C_P$  was just over 0.45 at  $\lambda \approx 3.5$ , was found to be for a 19 deg  
144 twist, as show in 1.



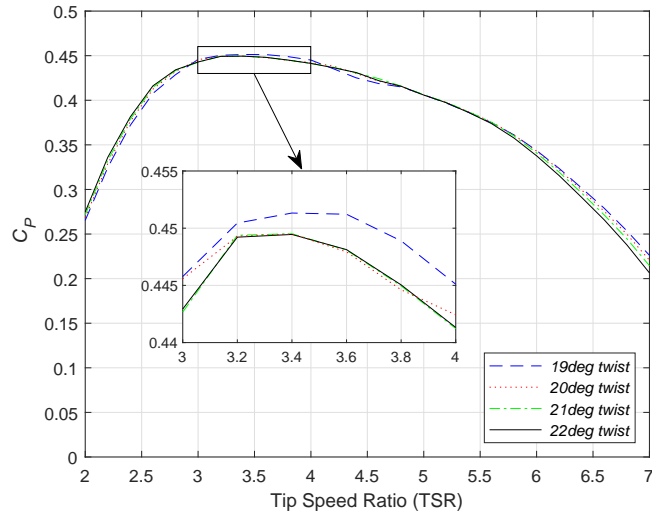


Figure 1: Comparison of the BEMT  $C_P$  predictions for twist distributions between 19-22 degrees

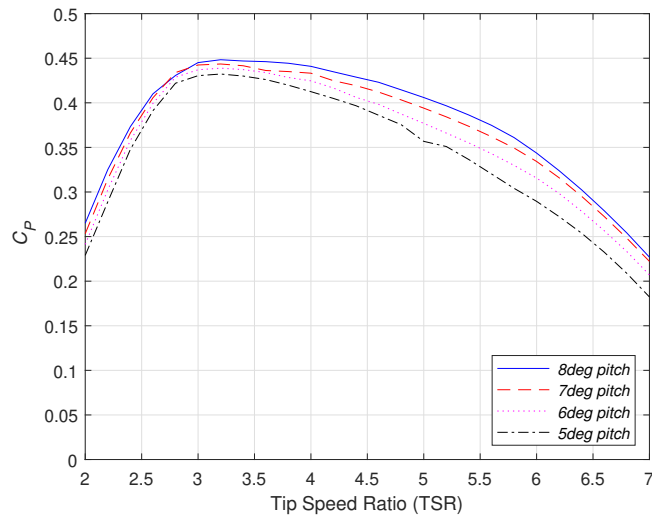


Figure 2: Comparison of the BEMT  $C_P$  predictions for pitch angles of 5-8 degrees

145 Finally a range of pitch angles between  $5^\circ - 8^\circ$  were studied in more  
 146 detail.  $C_P$  and  $C_T$ , for these pitch angles, can be seen in Figures 2 and 3,

147 respectively. The pitch angle of  $8^\circ$  was found to yield the highest  $C_P \approx 0.45$   
 148 with a  $C_T \approx 0.88$  at  $\lambda \approx 3.5$ .

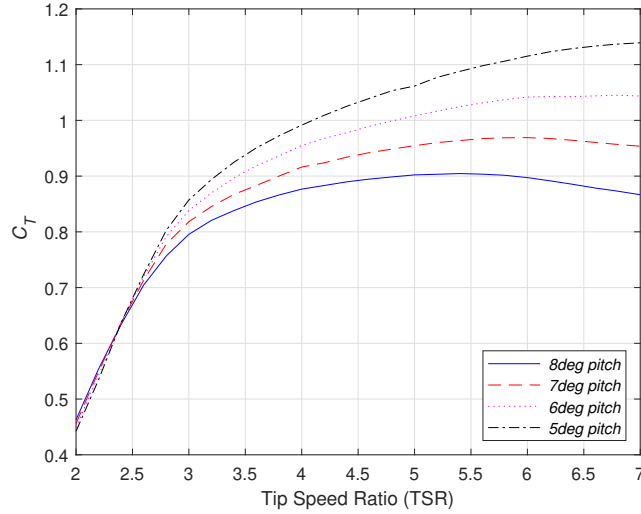


Figure 3: Comparison of the BEMT  $C_T$  predictions for pitch angles of 5-8 degrees.

### 149 3.2. Computational Fluid Dynamics

150 The optimised geometry, with a 384.5 mm blade length, was modelled  
 151 using ANSYS CFX. Approximately, 60 mm length of the blade, from the  
 152 root, was modified and blended with the Wortmann profile to enable the  
 153 blade to be connected to the turbine hub. The models developed all contained  
 154 a Moving Reference Frame (MRF), as sub domain which encompassed the  
 155 entire turbine rotor. The inclusion of the MRF facilitated simulation of the  
 156 turbine rotation. The width, depth and height of the overall fluid domains  
 157 were generated to replicate the geometries of the test facilities ultimately  
 158 used for turbine characterisation.

159 An outline of the CFD models are presented here, with details presented  
 160 in Table 1. However, further details can be found in [23]. Each blade was

161 divided into three sections: the blade tip, middle and root. The smallest  
 162 elements were concentrated at the tip, starting at 3 mm gradually increasing  
 163 to 7 mm at the root and hub. The growth rate, specifying the rate of cell size  
 164 growth, was set to 1.1, with the maximum element size set to 20 mm, which  
 165 resulted in 3 million elements, with around half of these elements contained  
 166 within the MRF. A  $1 \text{ ms}^{-1}$  plug flow boundary condition was applied to the  
 167 inlet of the model domain and a static pressure of 0 Pa at the outlet. The  
 168 walls, base, faces of turbine, hub and stanchion were all set to the no slip  
 169 condition with the top of the domain defined as an opening. The RANS  
 170 equations were closed using the SST  $k-\omega$  turbulence model as developed by  
 171 [24] and successfully applied to tidal turbine modelling in [13, 15, 16, 20].  
 172 A comparison made between the torque and thrust results from the steady  
 173 state and transient models showed less than 2% differences hence the steady  
 174 state model was used to reduce modelling time.

Table 1: CFD modelling information

<b>Model Name</b>		<b>No Stanchion</b>	<b>CNR-INM</b>	<b>IFREMER</b>
Geometry	Domain Dimensions	6[m] x 6[m] x 11[m]	9[m] x 3.5[m] x 20[m]	4[m] x 2[m] x 18[m]
	Stanchion	No	Yes	Yes
Set Up	Inlet	1[m/s]	1[m/s]	1.1[m/s]
	Outlet	Pressure 0[Pa]	Pressure 0[Pa]	Pressure 0[Pa]
	Walls	Free Slip	No Slip	No Slip
	Top	Free Slip	Opening	Opening
	Solver Type	Steady	Steady	Steady

175 The results from the CFD modelling along with the BEMT results are  
 176 presented in Figures 6 and 7. By comparing the BEMT to the CFD model  
 177 that includes the stanchion it can be seen that the BEMT generates higher  
 178 predictions for both the  $C_P$  and  $C_T$ , due to the stanchion not being taken into  
 179 consideration as part of the BEMT calculation. The flow directly behind the  
 180 blades will have a lower velocity due to the blockage effect of the stanchion  
 181 and ultimately reduce the performance of the blade passing the stanchion  
 182 [15]. If the stanchion is removed from the CFD model and compared with  
 183 the BEMT results, then a much closer comparison between both the thrust  
 184 and the power can be seen. The BEMT results also showed a lower  $\lambda$  value for  
 185 peak power. The authors suggest that this may be due to Reynolds effects  
 186 in matching the lift and drag coefficients, similar findings were presented in  
 187 [25].

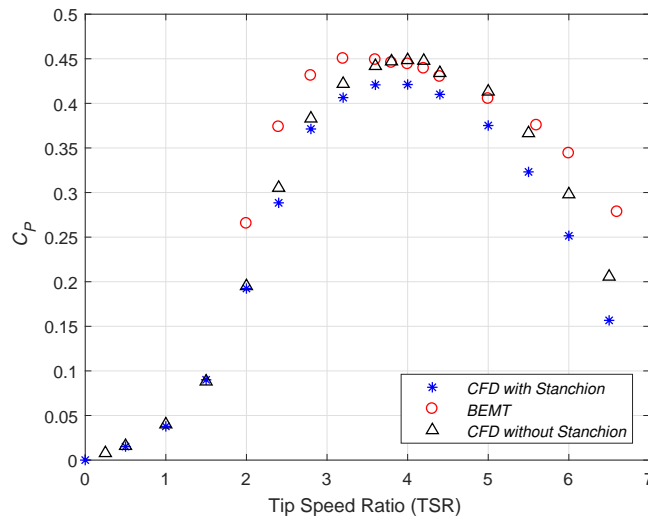


Figure 4: Comparison of the  $C_P$  between CFD and BEMT

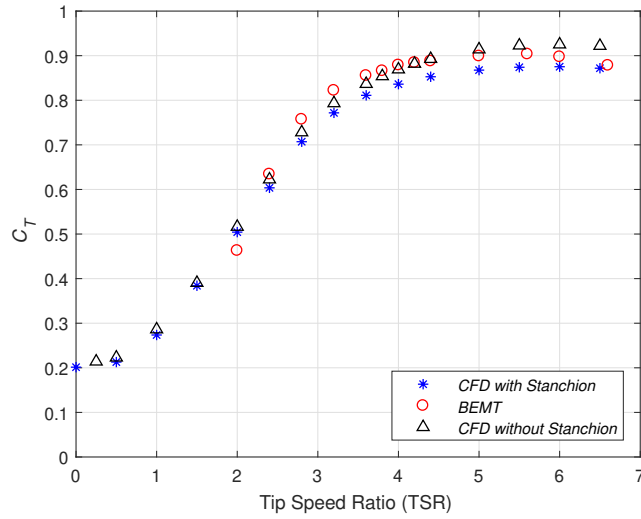


Figure 5: Comparison of the  $C_T$  between CFD and BEMT

Table 2: Overview of new rotor ( $D = 0.9m$ ) parameters used to develop the design specification.

Quantity	Rotor Value
Peak $C_P$	0.42 ( $\lambda \approx 4.0$ )
Peak $C_T$	0.88 ( $\lambda \approx 6.0$ )
Peak $C_q$	0.14 ( $\lambda \approx 2.0$ )
Freewheeling	$\lambda = 8$
Peak Power	293 W (110RPM)
Peak Thrust ( $U = 1.3ms^{-1}$ )	615 N (165RPM)
Peak Torque ( $U = 1.3ms^{-1}$ )	44 Nm (55RPM)
Max RPM at $1.3ms^{-1}$	220

## 188 4. Turbine Design

189 The following section details the design of the nacelle, drive train, elec-  
190 tronic machine and instrumentation generated to compliment the newly de-  
191 veloped blades forming a 1/20th instrumented HATT. The section is split  
192 into two parts. The first focusses on the design requirements for the turbine  
193 development and the second details the design solution developed to meet  
194 the outlined requirements.

### 195 4.1. Design Criteria

196 The specifications for the turbines are shown in Table 3A. The  $C_T$  and  
197  $C_P$  for the rotor geometry were used to develop the rated loadings and power  
198 output for the HATT design. As the CFD results hadn't been validated at  
199 this stage, a safety factor of 1.5 was applied to the rated quantities, at a  
200 mean flow velocity of  $1.3 \text{ ms}^{-1}$  and instantaneous velocities up to  $1.5 \text{ ms}^{-1}$   
201 (based on a turbulence intensity of 15%). This corresponds to a mean chord  
202 based Reynolds number,  $RE_{0.7Chord} = 8.44E + 4$  as defined in Appendix A.  
203 The design loads were based on the standard equations defined in Equations  
204 1 to 4.

Table 3: Table outlining the main design specifications and Instrumentation List for the developed HATT.

**A.**

Requirements List	
Specification	Details
Rated Flow Velocity	Continuous: $1.3 \text{ ms}^{-1}$ Instantaneous: $1.5 \text{ ms}^{-1}$
Rated Power	0.6 kW
Maximum Rotational Velocity	350 RPM
Rated Torque	Continuous: 41 Nm Instantaneous: 54 Nm
Maximum Rotor Thrust	1.07 kN
Maximum Blade Root Bending Moment	Flapwise: 129.76 Nm Edgewise: 18.13 Nm
Sample Rate Load Measurements	1032 Hz
Control Types	Speed Control (SC), Torque Control (TC) Regulated Torque Control Optimal $\lambda$ control

**B.**

Instrumentation List
Flap-wise and Edge-wise blade root bending moments (each blade); Rotor Thrust; Rotor Torque; Rotor Position; Rotational Velocity; PMSM Torque; Stanchion Bending Moment; Support Structure Vibration.

205 The diameter of the turbine was specified as 0.9m, this was in line with a  
206 1/20th scale HATT. A direct-drive device was decided upon, this was based  
207 upon the experience acquired during development of the legacy HATTs de-  
208 veloped by the authors and detailed in [14]. The turbine control and power  
209 take-off were to be undertaken by a PMSM. The power flow from the tur-  
210 bine and its associated braking torque were to be controlled by a drive series  
211 made up of back-to-back Voltage Source Converters (VSCs) either side of a  
212 DC bus. This decision was made based on the flexibility demonstrated when  
213 previously using such a set up. Previously closed-loop, set-point speed and  
214 torque control had been demonstrated. Furthermore, with the addition of  
215 outer control loops this set up could be utilised to achieve optimal power  
216 and torque control strategies allowing for more focused research into turbine  
217 loadings under representative control scenarios[26].

218 As the primary aim of the scale model HATT was for use in studying  
219 dynamic and transient loading characteristics, rotor load measuring instru-  
220 mentation was to be included. This ensured that the turbine was capable of  
221 providing dynamic,  $C_P$ ,  $C_T$  and  $C_\theta$  measurements directly associated with  
222 the turbine rotor. To compliment this the capability of measuring the dy-  
223 namic blade root bending moments, for each turbine blade, was incorporated.  
224 To allow for the high fidelity study of transient loading throughout a turbine  
225 rotation, sample rates were required such that one sample per  $2^\circ$  was col-  
226 lected at turbine free-wheeling for the rated fluid velocity of  $1.3 \text{ ms}^{-1}$ . Based  
227 on the power curves developed via CFD, free-wheeling was found to occur at,  
228  $\lambda \approx 8$ . At  $1.3 \text{ ms}^{-1}$  this corresponds to a free-wheeling rotational velocity of  
229 220 RPM or a sampling rate of 1324 Hz to fulfil the stipulated requirement.



230 Lastly, the requirement was stipulated of a maximum measurement uncer-  
231 tainty (for each instrument) of 5 % of the maximum loads measured for each  
232 instrument.

#### 233 *4.2. Design Overview*

234 A cross section of the turbine can be seen in the rendered SolidWorks  
235 image shown in Figure 6. The HATT power transfer mechanism utilises a  
236 direct-drive set-up with turbine control and power take-off undertaken by  
237 a Permanent Magnet Synchronous Machine (PMSM) controlled via back-  
238 to-back VSCs. The front section of the turbine was developed to house an  
239 instrumentation suite consisting of an integrated rotor thrust/torque trans-  
240 ducer, an encoder and an instrumented rotor. The instrumented rotor was  
241 developed to measure, 'flap-wise' and 'edge-wise' blade root bending mo-  
242 ments for each turbine blade.

243 Additional installed instrumentation includes a moisture sensor, stan-  
244 chion bending moment measurements and support structure vibration mea-  
245 surements. The instrumentation wiring is transferred into the rotational  
246 reference frame by an 18-way slip ring mounted on the turbine drive shaft.  
247 The turbine body is flanged together with the support stanchion through  
248 which the power, encoder and instrumentation cables are fed.

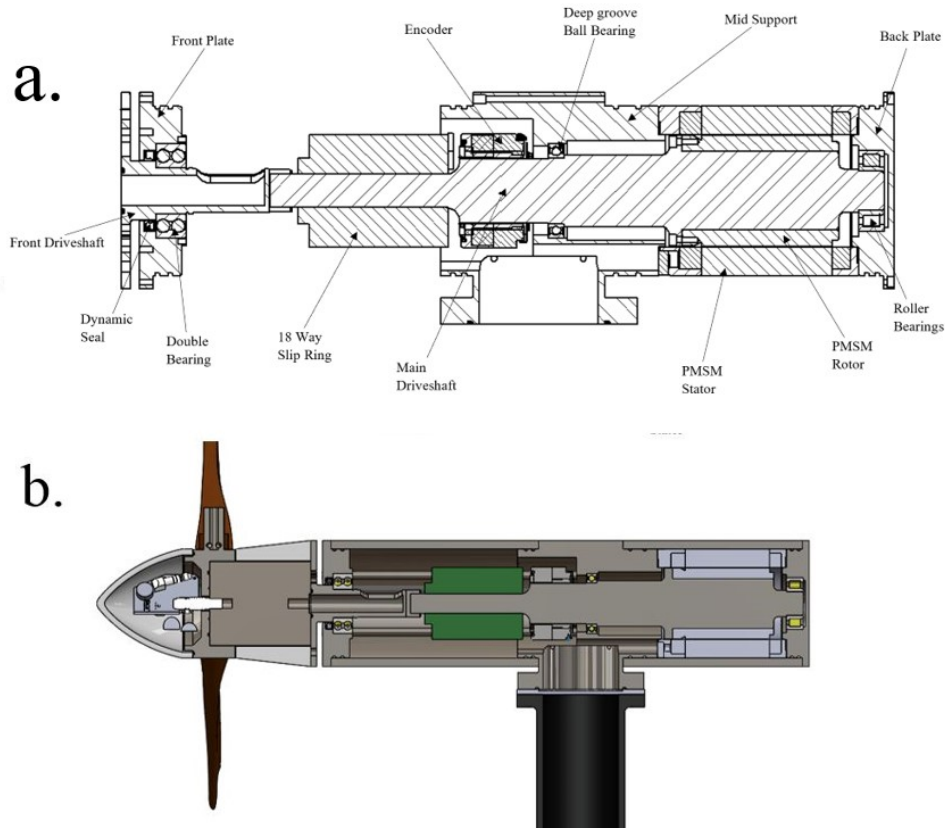


Figure 6: Solidworks rendering of the 1/20th scale HATT.

249 *4.3. Drive Train Design*

250 The turbine was designed as a direct drive HATT. As shown in Figure  
 251 6, it was created via two drive interfacing shafts to allow for the flanging  
 252 arrangement to the thrust/torque transducer. Using two drive shafts also fa-  
 253 cilitated the positioning of the PMSM on back side of the turbine away from  
 254 the rotor instrumentation. The structure of the design was created to intro-  
 255 duce modularity into the design to allow for instrumentation developments  
 256 and ease of part replacement. The design decision to position the PMSM at

257 the back end of the HATT was also undertaken to reduce electrical noise in  
258 the measurement readings.

259 The drive shaft was supported by three bearing housings; the mid sup-  
260 port, front and back plates. The first shaft has a hollowed section to accom-  
261 modate instrumentation cabling, which was fed from the rotating portion of  
262 the 18-way slip ring. The front shaft was supported by double row bearings,  
263 which act as the main thrust bearing and are housed in the front plate. A  
264 dynamic seal was embedded in the front plate to protect from water ingress.

265 The main drive shaft was supported in two places, at the mid support and  
266 back plate. The front and back drive shafts are coupled together to transfer  
267 torsional loads and rotational motion. The main shaft has been fitted with  
268 an encoder and slip ring to the left of the mid plate and a PMSM to the right  
269 of the mid plate with respect to Figure 6.

#### 270 *4.4. Permanent Magnet Synchronous Machine, Drives and Control*

271 The model scale HATT houses an embedded PMSM for turbine breaking  
272 and control. The PMSM used was a Bosch Rexroth MST 130E. The ratings of  
273 the motor are presented in Table 4. The motor was chosen for its relative high  
274 torque capacity for a non-directly cooled motor as required by the direct-drive  
275 configuration. The rotor of the PMSM houses permanent magnets arranged  
276 into 10 pole pairs and was mounted on the back drive shaft fastened via a  
277 flange. The stator contains the motor windings and was integrated via the  
278 mid-section and back plates of the HATT. To cool the motor appropriately,  
279 the motor was aligned and fitted into the stainless steel nacelle of the HATT.  
280 Circular steps on the mid-section and back plate align the stator relative to  
281 the drive shaft to preserve the air gap of 0.4 mm.

282 Power flow to and from the PMSM was managed by a drive section,  
283 which was located in a cooled drive cabinet. The drive sections are made  
284 up of a mains choke, a mains filter, a rectifier and an inverter. A three  
285 phase connection was made to the mains choke which manages regenerative  
286 energy feedback into the grid when required. The three phase connection  
287 was the made between the mains choke and the mains filter, filtering was  
288 undertaken to maintain power quality in the supply to the rectifier. The  
289 filtered three phase connection was then fed to a rectifier where the AC  
290 current was converter to DC via a VSC with a switching frequency of 4000  
291 Hz. The rectifier and inverter are connected via a DC bus integrated with  
292 a DC bus capacitor. The inverter then creates a three phase AC current  
293 which was connected to the motor. The power flow to and from the motor  
294 are managed by the VSCs either side of the DC bus - similar to back-to-back  
295 set up used for HATTs and wind turbines adopting a direct-drive PMSM  
296 topology. The back-to-back VSCs allow for servo based Vector Oriented  
297 control of the turbine to directly the torque required of the PMSM or via an  
298 additional velocity control loop the desired rotational velocity. The encoder  
299 required for servo-control of the PMSM is detailed in Section 4.5.3.

#### 300 *4.5. Instrumentation*

301 An instrumentation suite was integrated into the turbine in order to quan-  
302 tify dynamic loadings on the HATT under various fluid flow regimes. An  
303 overview of the instrumentation suite integrated into the turbine is presented  
304 below.

Table 4: The motor parameters for the Bosch Rexroth MST130E.

<b>Motor Parameters</b>	
Rated Torque	42 Nm
Maximum Speed	350 RPM
Rated Power	0.6 kW
Maximum Rotational Velocity	350 RPM
No. of Pole Pairs	10
Winding Resistance	14.9 $\Omega$
Mass of Stator	7.7 kg
Mass of Rotor	2.2 kg

305 *4.5.1. Rotor Torque and Thrust Transducer*

306 A bespoke rotor torque and thrust transducer was created by Applied  
 307 measurements Ltd. The transducer used was an adapted DBBSS/TSF Torque  
 308 and Axial Force Sensor, which had a rated maximum thrust load of 1.8 kN  
 309 and a maximum rated torsional loading of 100 Nm. The transducer was  
 310 adapted for the specified load rating, for waterproofing, to house two 18 way  
 311 Lemo EGG.2B.318 connectors and to accommodate through wiring for hub  
 312 instrumentation. The transducer was fastened between the front drive shaft  
 313 and the turbine rotor upstream of any bearings or seals to measure rotor  
 314 loads prior to any drive shaft losses. The transducer used two ICA4H am-  
 315 plifiers, one for thrust loading with a sensitivity of 0.005 mA/N and one for  
 316 torque loading with a sensitivity of 0.08 mA/N, both amplifiers were housed  
 317 in the body of the transducer.

318 *4.5.2. Instrumented Hub*

319 The turbine hub was created to house the blades and measure both flap-  
320 wise and edge-wise bending moments on each of the three turbine blades.  
321 The hub is a circular section with holes for flange fixing to the thrust/torque  
322 transducer, a bore in the centre accommodates a Lemo connector for instru-  
323 mentation wiring. Three 'bosses' project radially from the outside of the  
324 circular section, to which the blades are attached via grub screws. Each of  
325 the bosses were spaced at  $120^\circ$  and each of the bosses houses two full-bridge  
326 strain gauge set ups for measuring blade root bending moments.

327 The boss sizes were set such that they limited the stress on the machined  
328 faces to 30% of the material yield stress, whilst setting a suitable strain level  
329 on the faces.

330 *4.5.3. Encoder*

331 The encoder selected, and used for position feedback, was an optical  
332 encoder, the model utilised was the Heidenhain ENC113 encoder with Endat  
333 2.2 interfacing. The encoder is of 13 bit type with a quoted system accuracy  
334 of  $\pm 20$  seconds of arc.

335 *4.5.4. Amplification and Signal Processing*

336 The blade load and thrust/torque transducer measurements all utilised in-  
337 tegrated circuit ICA4H amplifiers. The output of the amplifiers was between  
338 4 mA and 20 mA and can accommodate bridge systems with sensitivities be-  
339 tween 0.5 mV/V and 150 mV/V. A gain setting resistor was used to achieve  
340 measurements in the 4 mA to 20 mA range for differing bridge sensitivities.  
341 The amplifier required 24 V input and outputs a regulated 5 V supply to

342 the wheatstone bridge configurations. The amplifier has an inbuilt low-pass  
343 filter with a fixed cut-off frequency of 1 kHz.

344 The stanchion bending moment instrumentation, consisting of a full-  
345 bridge configuration of strain gauges, was amplified and filtered by a PCM  
346 Strain Gauge Amplifier(SGA). The PCM SGA was set to filter the amplifier  
347 output at 1 kHz. Lastly, the piezo-electric vibration sensors signals are not  
348 amplified and are filtered at the NI9234 DAQ card by a low pass filter with  
349 the cut-off frequency set to set to 5kHz. The low pass filters cut-off values  
350 are set to act as an anti-aliasing filter to ensure quality of transient analysis  
351 of the captured loading and vibration data. Table 5 shows the sample rate  
352 and anti-aliasing filter cut-off frequency for each piece of instrumentation.

#### 353 *4.5.5. Data Acquisition*

354 Data acquisition for all three turbines was undertaken via a National  
355 Instruments Compact RIO. The DAQ cards used in the compact RIO are  
356 outlined in Table 5. The table shows the measurement type, bit depth, sam-  
357 ple rate and anti-aliasing filter cut-off frequency for each of the channels. A  
358 Compact RIO was utilised due to the advantages of being able to utilise both  
359 the Field Programmable Gate Array (FPGA) and the Real-Time operating  
360 system for test control and data capture and management. The tasks under-  
361 taken by the Compact RIO have been broadly split into data capture and  
362 triggering, which was undertaken by the FPGA and data management and  
363 test control which was undertaken by the Real-Time operating system.

Table 5: Table outlining the NI DAQ cards used for data capture along with information on the measurement type, bit depth, sample rate and anti-aliasing filter cut-off frequency.

Measurement Type	DAQ Card	Bit Depth	Sample Rate	Low Pass Cut-off
Blade root bending moment	NI9203	16-Bit, 0-20 mA	2 kHz	1 kHz
Rotor Thrust	NI9203	16-Bit, 0-20 mA	2 kHz	1 kHz
Rotor Torque	NI9203	16-Bit, 0-20 mA	2 kHz	1 kHz
Stanchion Bending Moment	NI9207	24-Bit, 0-10 V	2 kHz	1 kHz
Stanchion Vibration	NI9234	24-Bit, 0-100 mV	10 kHz	5 kHz

364 *4.6. Waterproofing and Moisture Sensor*

365 Figure 7 shows an overview of the sealing arrangement for the main tur-  
 366 bine assembly. Generally, sealing of the turbine was accomplished using O-  
 367 rings, with O-ring sizing and groove specification undertaken following the  
 368 BSI 4518 British standard. As mentioned a dynamic seal was utilised to  
 369 seal around the entry point of the front drive shaft into the turbine nacelle  
 370 through the front plate.

371 An interlock moisture sensor was integrated into the turbine to alert the  
 372 user in the event that any of the outlined sealing arrangements failed and  
 373 water ingress into the turbine occurred. This feature was required for both  
 374 safety and to protect the scale model HATT hardware. The circuit was  
 375 connected to 10 V source, output from the Compact RIO; in the event of  
 376 water ingress the two moisture probes are shorted or connected together.  
 377 The shorting of the two probes changes the circuit output from 10 V to 0V  
 378 (ground). A 0 V reading from the moisture sensor then starts an automatic



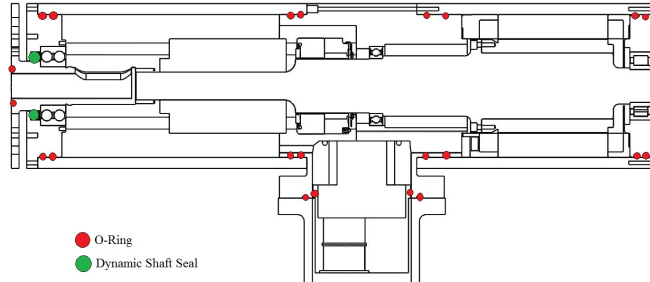


Figure 7: Overview of the sealing arrangements for the 1/20th Scale HATT.

379 shut down of the turbine PMSM to avoid any electrical damage. Lastly, the  
 380 user would be alerted of the leak so the turbine can be removed from the tow  
 381 tank or flume.

## 382 5. Turbine Characterisation Testing

383 Initially, a single turbine, Turbine T1, was manufactured and tested.  
 384 Once this turbine was validated in terms of design and operation the fur-  
 385 ther two turbines, T2 and T3, were constructed. As such, turbine testing  
 386 was conducted in 3 stages:

387 **Stage 1:** Testing undertaken to provide validation of the design and  
 388 characterisation data for a single turbine over the full working  $\lambda$  range. This  
 389 testing, funded by Marinet 2, was undertaken at the CNR-INM wave-tow  
 390 tank in Rome, Italy. This allowed for characterisation of the turbine with  
 391 and without defined waves at controlled speeds with no turbulence present.  
 392 In addition, testing of the turbine's ability to operate under speed or torque  
 393 control was conducted.

394 **Stage 2:** The single turbine was then tested in the IFREMER wave-  
 395 current flume facility in Boulogne-Sur-Mer, France, again with and without

396 waves. This allowed for a low turbulence level and a range of flow speeds,  
397 again over the full  $\lambda$  range.

398 **Stage 3:** With the turbine design validated, the second and third turbines  
399 were manufactured and tested in the Kelvin Hydrodynamics Laboratory  
400 (KHL) tow tank, in Glasgow.

401 Table 6 shows an overview of the experimental parameters for each facility.  
402 It should be noted that differing pitch angles were used for the IFREMER  
403 and KHL cases, this was done to test the effects of differing pitch angles and  
404 to understand the repeatability of the pitch angle setting procedure.

Table 6: Table providing an overview of peak non-dimensional quantities observed across the differing test facilities for Turbine 1 (T1).

<b>Qty</b>	<b>CNR-INM</b>	<b>IFR</b>	<b>KHL</b>
Facility Type	Tow Tank	Flume Tank	Tow Tank
Testing Data	November 2017	April 2018	February 2019
Data Record Length	90s	100s	60s
Facility Dimensions	$9 \times 3.5 \times 220$ m	$4 \times 2 \times 14$ m	$4.6 \times 2 \times 76$ m
Blockage Ratio	2.8 %	8.0 %	6.9 %
Turbine Depth	1.5 m	1 m	1 m
Pitch Angle	$8.0^\circ$	$6.2^\circ$	$6.2^\circ$
Flow/ Carriage Velocities	$1.00 \text{ ms}^{-1}$	$0.50 \text{ ms}^{-1}$ $0.60 \text{ ms}^{-1}$ $0.90 \text{ ms}^{-1}$ $1.00 \text{ ms}^{-1}$ $1.05 \text{ ms}^{-1}$ $1.10 \text{ ms}^{-1}$ $1.20 \text{ ms}^{-1}$ $1.30 \text{ ms}^{-1}$	$0.80 \text{ ms}^{-1}$ $1.0 \text{ ms}^{-1}$ $1.2 \text{ ms}^{-1}$

405 *5.1. CNR-INM Testing*

406 The Stage 1 tests were undertaken at the CNR-INM wave tank. The  
407 tests were conducted by attaching the model HATT to the carriage and  
408 towing it along the tank as shown in Figure 8A. The tests were undertaken to  
409 characterise the HATT and to confirm its correct operation. A series of tests  
410 were undertaken all with the carriage velocity set to  $1 \text{ ms}^{-1}$  ( $RE_{0.7chord} =$

411  $6.48 \times 10^4$ ). A 0.09 m diameter stanchion held the turbine in place to the  
412 tow carriage. The turbine hub centre was set at 1.5 m below the still water  
413 surface, and centred in the cross-stream direction. Cables from the turbine  
414 were run inside the stanchion to the control and data acquisition systems  
415 situated on the carriage. For this set of tests the pitch angle for each blade  
416 was set to  $8^\circ \pm 0.5^\circ$ . The tests were undertaken with both speed and torque  
417 control over the range of operating  $\lambda$  values. Prior to each test a zero reading  
418 was taken to confirm no drift in the instrumentation had occurred.

## 419 *5.2. IFREMER Testing*

420 The Stage 2 test campaign was undertaken at the flume tank facility in  
421 Bolougne-Sur-Mer in France. Again a major aspect of this testing was to  
422 characterise the turbine performance. In this instance the turbine blades  
423 were set to a pitch angle of  $6.2^\circ \pm 0.5^\circ$ . The turbine was supported via the  
424 same stanchion arrangement as the CNR-INM testing described in Section  
425 5.1, albeit with different supporting bracket arrangement. The setup can be  
426 seen in Figure 8B. The turbine in this case was submerged to a depth of 1 m  
427 meter and again centralised in the cross stream direction. A Laser Doppler  
428 Velocimeter (LDV) was setup to measure the fluid velocity in the stream-  
429 wise and cross-stream directions. The measurement volume of the LDV was  
430 aligned with the centre of the turbine nose cone, 1 m upstream.

431 In this instance the turbine was characterised under a variety of fluid  
432 velocities ranging between  $0.5 \text{ m s}^{-1}$  ( $Re_{0.7Chord} = 3.25 \times 10^4$ ) and  $1.3 \text{ m s}^{-1}$   
433 ( $Re_{0.7Chord} = 8.44 \times 10^4$ ). A honeycomb flow straightener was used at the  
434 flow inlet to straighten the flow and reduce the turbulence levels, with prior  
435 characterisation of the fluid flow under this set up finding turbulence intensi-

436 ties of approximately 2%. Similarly to the testing undertaken at CNR-INM,  
437 both speed and torque control methods were utilised with a variety of rota-  
438 tional velocities and feedback torques applied to test the turbine at a variety  
439 of  $\lambda$  values.

### 440 *5.3. Kelvin Hydrodynamics Laboratory testing*

441 Stage 3 testing was undertaken at the Kelvin Hydrodynamic laboratory,  
442 the turbine set-up prior to lowering to the 1 metre depth can be seen in  
443 Figure 8C. The tests were undertaken to individually characterise the three  
444 HATTs, to confirm their correct operation and provide a comparison with  
445 each other. An initial series of tests were undertaken for 8  $\lambda$  settings with  
446 carriage speeds of 0.8, 1.0 and 1.2  $ms^{-1}$  ( $Re_{0.7Chord} = 5.184 \times 10^4$ ,  $6.48 \times 10^4$   
447 and  $7.76 \times 10^4$  respectively), with speed control. The turbine hub centre  
448 was set 1.0 m below the still water surface and centred in the cross-stream  
449 direction. Cables, were again, run along the inside of the stanchion from the  
450 turbines and connected to the control and data acquisition systems situated  
451 on the carriage. For this set of tests the pitch angle for each blade was set  
452 to  $6.2^\circ \pm 0.5^\circ$ . On completion of the speed control experiments a series of  
453 tests were then completed using torque control. As with all tow tank testing  
454 described in this paper prior to each, for each turbine, a zero reading test  
455 was undertaken to confirm no drift in the instrumentation had occurred.

### 456 *5.4. Results*

457 The results section presents the data recorded during the aforementioned  
458 testing campaigns with a focus on two aspects: the characterisation of turbine  
459 T1 during testing at three differing facilities, Section 5.4.1, and a comparison

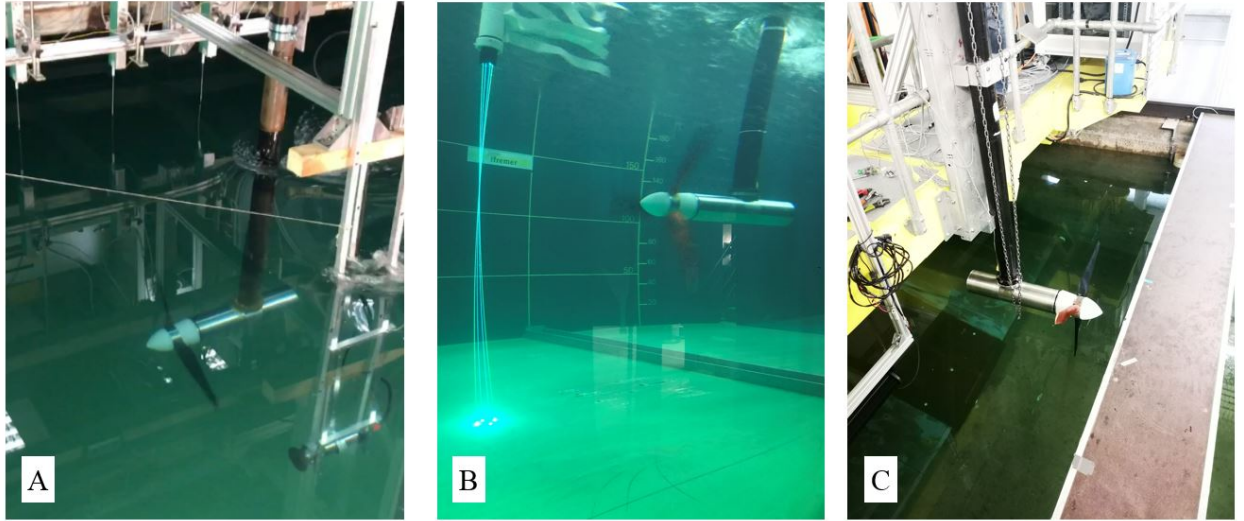


Figure 8: The test setups at the various testing facilities, A) CNR-INM, B) IFREMER and C) KHL.

460 between the results obtained for each of the three turbines tested at KHL,  
 461 Section 5.4.2.

#### 462 5.4.1. Single Turbine Calibrations

463 Figures 9 and 10 show a comparison between the results obtained dur-  
 464 ing the CNR-INM, IFREMER and KHL test campaigns for turbine T1 and  
 465 a flow velocity of  $1 \text{ ms}^{-1}$ . A comparison was made between the raw and  
 466 non-dimensional analogues of the power, torque and thrust developed by the  
 467 turbine. Data for both speed and torque control strategies have also been  
 468 included for the test campaigns undertaken at both CNR-INM and IFRE-  
 469 MER. The non-dimensional coefficients were calculated using equations 1 to  
 470 4. Power and torque, along with the non-dimensional equivalents, were cal-  
 471 culated for this comparison using the measured PMSM winding currents, as

472 the rotor torque transducer was not available during the CNR-INM testing  
473 campaign. The PMSM winding current measurements were decomposed into  
474 direct and quadrature axis currents, the quadrature axis currents were then  
475 scaled to give the braking torque applied by the PMSM - in this regard it  
476 should be noted that these measurements included drive shaft losses. In the  
477 cases of the CNR-INM and KHL facilities, the fluid velocity used in the cal-  
478 culations was the carriage velocity. In the case of the IFREMER testing, the  
479 fluid velocity used to calculate the non-dimensional power coefficients was  
480 the swept-area averaged fluid velocity.

481 As the differing facilities had differing cross-sectional areas, see Table  
482 6, flow around the turbine would have been constrained and accelerated to  
483 differing degrees, resulting in artificially exaggerated turbine performances  
484 being recorded. As such, the non-dimensional parameters were corrected to  
485 account for the differing blockage ratios in the differing facilities. This was  
486 done by estimating the ratio of blockage constrained flow velocity to open  
487 channel flow velocity,  $U/U_f$ , using the method detailed in [6]. The ratios  
488 developed are plotted in Figure 9 against  $\lambda$  values for the differing facilities.  
489 The aforementioned ratio was squared and cubed before applying as a factor  
490 to the non-dimensional thrust and power coefficients, respectively. Table 7  
491 shows the peak non-dimensional values obtained for turbine T1 during the  
492 three stages of testing described.

493

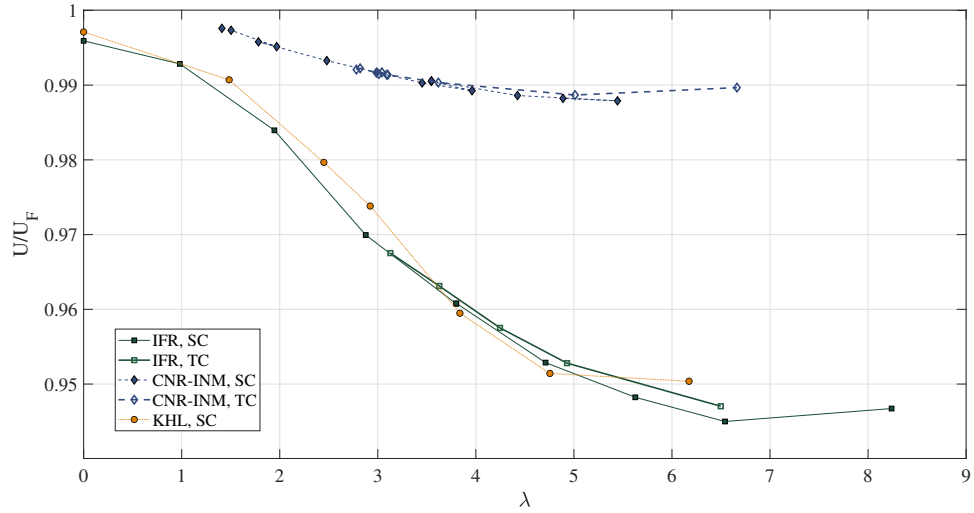


Figure 9: Figure showing the blockage ratio of constrained flow to open channel flow velocity,  $U/U_f$ , against  $\lambda$  values for the three differing test facilities.

Table 7: Table providing an overview of peak, blockage corrected non-dimensional quantities observed across the differing test facilities for Turbine 1 (T1).

Qty	CNR-INM	IFR	KHL
Max $C_P$	0.38	0.35	0.37
$\lambda$ @ Max $C_P$	3.55	3.13	2.92
Max $C_\theta$	0.134	0.119	0.141
$\lambda$ @ Max $C_\theta$	2.5	2.9	2.5
Max $C_T$	0.86	0.94	0.94
$\lambda$ @ Max $C_T$	5.5	6.5	6.2

494 Table 7 shows that relatively good agreement was found in the maximum  
495 power, torque and thrust coefficients measured. However, it should be noted  
496 that a lower power coefficient was recorded for the IFREMER test cases,



497 as well as discrepancies in the  $\lambda$  values recorded for peak power. Further  
 498 to this, a slightly lower  $C_\theta$  value was also recorded for the IFREMER test  
 499 case. Better agreement was seen in the  $\lambda$  value of peak torque coefficient. A  
 500 lower value of thrust coefficient was observed, as expected, for the CNR-INM  
 501 testing. This was likely due to the differing pitch angle setting for the CNR-  
 502 INM test and helps confirm that in the region of pitch angles varying between  
 503  $6^\circ$  and  $9^\circ$  a greater sensitivity in thrust loading is observed in contrast to a  
 504 relatively invariant power coefficient, as discussed in Section 3.

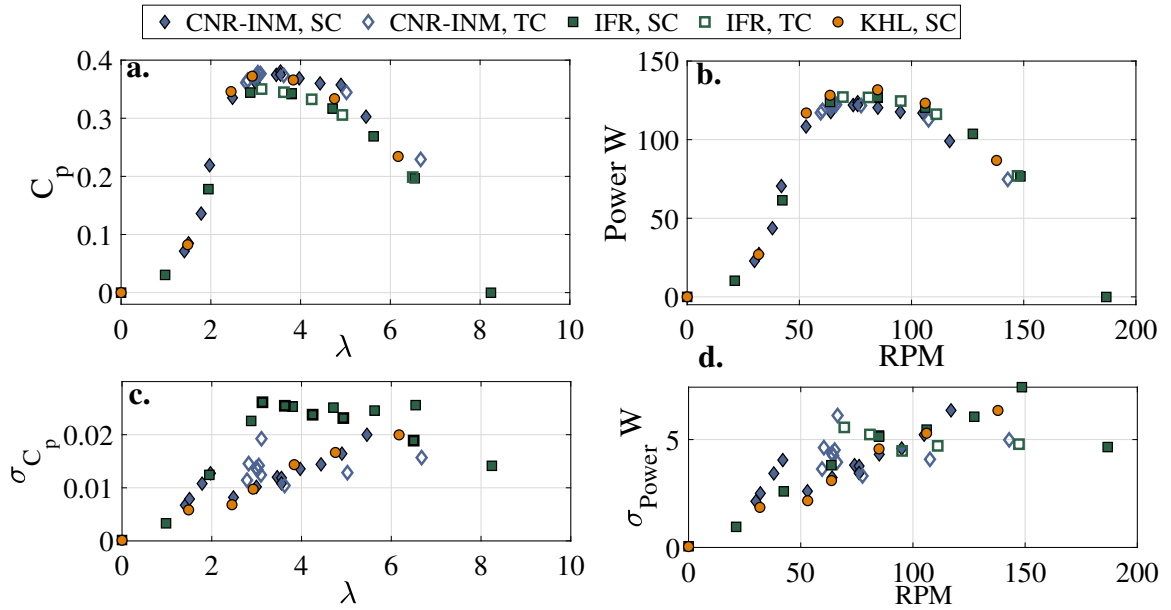


Figure 10: Blockage corrected power curves obtained whilst testing at CNR-INM, IFREMER and KHL. a) Shows Non-Dimensional power coefficient against  $\lambda$ . b) Shows Power against RPM. c) Shows the standard deviation in non-dimensional power coefficient against  $\lambda$ . d) Shows the standard deviation of power against RPM.

505 Inspection of the power curves, in Figure 10, shows that the IFREMER  
 506 test cases yielded a generally lower performance curve than the CNR-INM

507 and KHL test cases. Comparison of Figures 10a and 10b shows the block-  
508 age correction has a significant effect. Whilst the highest power capture was  
509 observed for the KHL cases, the blockage correction yields  $C_P$ -curves of a  
510 similar level for the CNR-INM and KHL cases. The discrepancy between  
511 the IFREMER  $C_P$ -curve and CNR-INM and KHL  $C_P$ -curves is likely to be  
512 due to greater drive-train losses during the IFREMER test. A change of  
513 dynamic seal between the CNR-INM and IFREMER testing campaigns was  
514 undertaken which could explain the deviation. Furthermore, it is also possi-  
515 ble that the change in the losses across the differing facilities may have altered  
516 the power capture to thrust relationship exploited in the blockage correction  
517 approach. This may have led to a distortion in the blockage correction factor  
518 applied in the case of the IFREMER tests.

519 It can be seen in Table 7 that the  $\lambda$ -value associated with maximum power  
520 performance varies between facilities - this is likely to be a result of the  $C_P$ -  
521 curve shape than any inherent difference between the facilities. Explicitly,  
522 this is due to the relatively flat shape of the characteristic  $C_P$  curve in the  
523 peak region as shown in Figure 10a. This may have been exacerbated by the  
524 differing  $\lambda$  values tested for each of the differing test campaigns.

525 The maximum standard deviation of power and  $C_P$  were of the order of  
526 3 and 3.5 % of the mean values obtained, respectively. The variability of the  
527 power produced by the turbine generally increased with rotational velocity  
528 as shown in Figures 10c and 10d. The dominant factor in this increase is  
529 the nature of how the power is calculated as the product of two measured  
530 quantities (PMSM braking torque and rotational velocity), this leads to the  
531 product of mean rotor velocity and torque variability becoming dominant in

532 power variability, explaining the dependence on rotor velocity. Similar values  
 533 for the variability in power and non-dimensional power coefficients were ob-  
 534 served for all test cases. Higher variability was expected for the IFREMER  
 535 test cases due to the presence of turbulence effects in these test cases. This  
 536 finding would suggest that the variability in power production measured via  
 537 the motor currents is dominated by measurement noise (common in motor  
 538 current measurements) and associated PMSM control functions rather than  
 539 the presence of low level turbulence. Lastly, the effect of torque control  
 540 rather than speed control seems to have made little difference to the mean  
 541 and standard deviations which are similar in magnitude for like facilities.

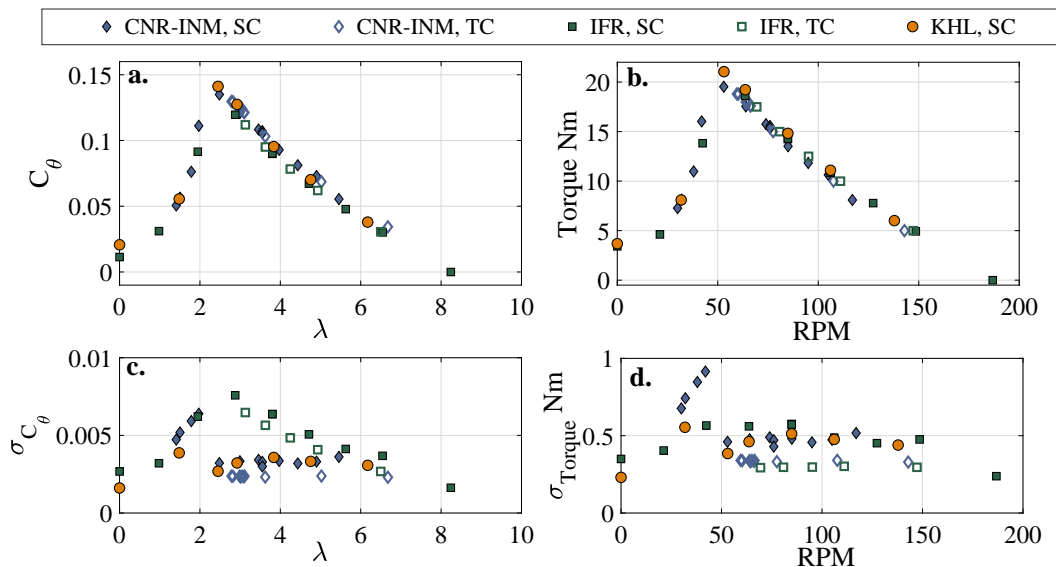


Figure 11: Blockage Corrected torque curves obtained whilst testing at CNR-INM,IFREMER and KHL. a) Shows Non-Dimensional torque coefficient against  $\lambda$ . b) Shows torque against RPM. c) Shows the standard deviation in non-dimensional torque coefficient against  $\lambda$ . d) Shows the standard deviation in torque against RPM.

542 Figure 11 shows that good agreement was found when comparing the

543 torque measurements from each facility. The blockage correction has had  
544 a significant effect on the  $C_\theta$  curves, which has resulted in very similar  $C_\theta$   
545 values for the CNR-INM and KHL test campaigns despite lower torsional  
546 values being recorded at CNR-INM, as shown by contrasting Figures 11a and  
547 11b. It can be seen in Figure 11a that the slight lower  $C_\theta$  value, presented  
548 in Table 7 for the IFREMER test case arises due to the operating points  
549 measured. It can be seen that the measurement points fall either side of  
550 peak torque, at  $\lambda \approx 2.5$  for the IFREMER test cases - although the shape of  
551 the curves observed for all facilities are similar.

552 The maximum standard deviation of torque and torque coefficients were  
553 of the order of 2 and 3 % of the mean values obtained, respectively. It  
554 can be seen that variability in torque produced by the rotor is of similar  
555 magnitude for each facility for  $\omega$ -values greater than  $\omega = 50$  RPM. Below this  
556 value all test cases show an increasing torque variability with increasing  $\omega$ ;  
557 the CNR-INM cases show the most severe torsional variability towards peak  
558 torque. In Figure 11d, it can be seen that the torsional variability was slightly  
559 higher for speed control cases than torque control cases, this is reflected in  
560  $C_\theta$  variability shown in Figure 11c. It can be seen that the variability in  
561  $C_\theta$  values measured at IFREMER follows closely the shape of the torque  
562 curves developed and shows generally higher variability, especially between  
563  $2 < \lambda < 6$ . This shows the dependence on the flow velocity variability  
564 when calculating  $\sigma_{C_\theta}$  via the standard variance propagation equations for  
565 independent variables. The similar levels of variability in torque for all speed  
566 control cases would suggest, again, that variability related to motor control  
567 is dominant over variability observed due to turbulence effects in the flume.

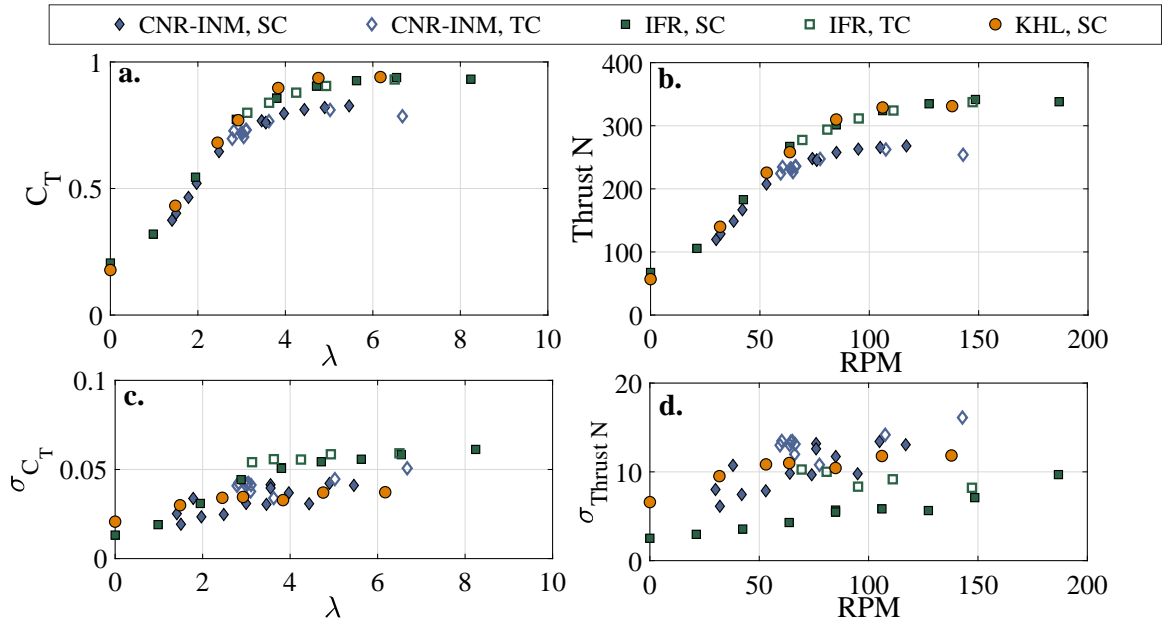


Figure 12: Blockage corrected thrust curves obtained whilst testing at both CNR-INM and IFREMER. a) Shows Non-Dimensional thrust coefficient against  $\lambda$ . b) Shows thrust against RPM. c) Shows the standard deviation in non-dimensional thrust coefficient against  $\lambda$ . d) Shows the standard deviation in thrust against RPM.

568 In Figure 12a and 12b the differing pitch settings between the CNR-INM  
 569 tests and the IFREMER and KHL cases are immediately apparent. Both the  
 570 raw thrust and blockage corrected non-dimensional thrust coefficient curves  
 571 show excellent agreement for the IFREMER and KHL cases. The  $C_T$  vs  $\lambda$   
 572 curve for CNR-INM are in agreement with the curves recorded from the other  
 573 facilities until approximately  $\lambda = 3.5$ , after this point the curves deviate in  
 574 shape with the CNR-INM curve becoming concave in shape as a drop-off in  
 575 thrust is observed at higher  $\lambda$ -values.

576 Again maximum standard deviation of thrust and thrust coefficients were  
 577 of the order of 3 and 3.5 % of the median values obtained, respectively. Inter-

578 esting, the variability in thrust for the tow tank cases measured was found to  
579 be higher than those observed in the flume test cases. This unexpected result  
580 would suggest that the variability in the thrust loading observed at CNR-  
581 INM is driven by a combination of potential tow carriage velocity precision,  
582 measurement noise and potential rotor imbalance. This is supported in that  
583 relatively similar standard deviations in the thrust coefficient were observed  
584 at the IFREMER test facility for similar levels of turbulence and reported in  
585 [27]. Regarding the CNR-INM data, intermittent noise spikes were observed  
586 in the thrust data. To combat this additional shielding was added between  
587 testing at CNR-INM and IFREMER. Regarding the root causes of the unex-  
588 pected variability observed at KHL, further analysis will be required to fully  
589 understand the unexpected result. Lastly, both thrust and non-dimensional  
590 thrust coefficient are affected by the control strategy adopted, exhibiting  
591 slightly higher thrust variations under the torque control cases which has  
592 been observed previously [19][26].

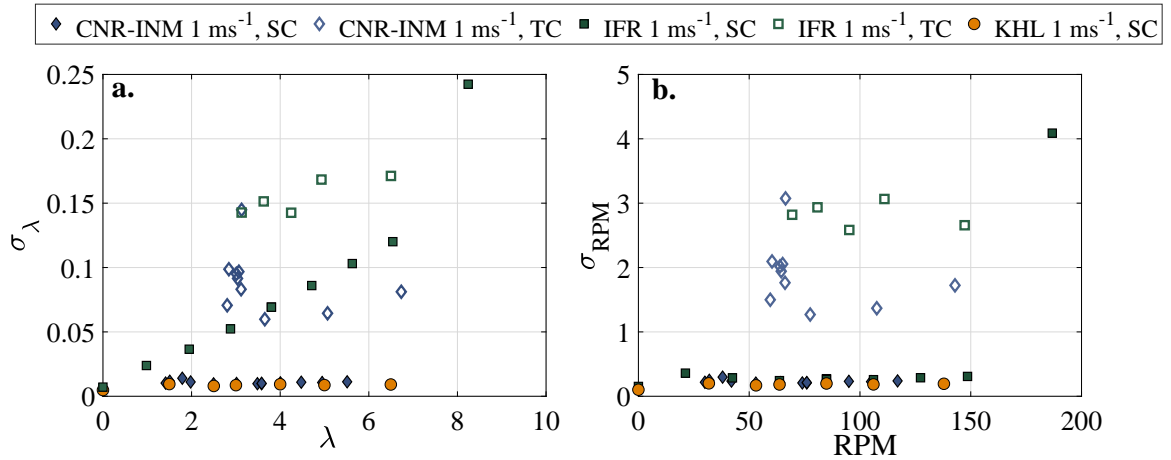


Figure 13: Figure showing the standard deviation of  $\lambda$  values against  $\lambda$  (left) and the standard deviation of RPM against RPM (right).

593 Figure 13 shows the standard deviation of the  $\lambda$ -values and RPMs ob-  
 594 served at each of the facilities. It is immediately clear that the control  
 595 strategy has major effect on the variability of the turbine operating point  
 596 during testing - this is in agreement with the higher thrust and torque fluc-  
 597 tuations observed for the torque control case. A discrepancy between the  
 598 non-dimensional kinematic quantity  $\lambda$  and the RPM standard deviations is  
 599 exhibited for the IFREMER test case. The increasing trend in standard de-  
 600 viation observed in Figure 13a would seem to be generated in the variance  
 601 propagation calculations made. This would suggest that covariance between  
 602 quantities is significant and should be used in such calculations.

#### 603 5.4.2. Three Turbine Characterisation at KHL

604 Figures 14 to 18 show the data sets for the three turbines tested at the  
 605 KHL providing the characteristic curves of  $C_P$ ,  $C_\theta$ ,  $C_T$ ,  $M_x$  and  $M_z$  for the  
 606 0.8, 1.0 and 1.2  $m s^{-1}$  carriage velocity cases. The plots are based on the rotor

607 and blade transducer data recorded; in addition  $C_P$  and  $C_\theta$  derived utilising  
608 PMSM winding current measurements are also presented, which clearly show  
609 the drive train losses. Spline fits to the data have been included for clarity  
610 and to highlight the underlying nature of the characteristic curves measured.  
611 Table 8 shows the peak quantities observed in the rotor data. Table 8 also  
612 shows the maximum standard deviation observed for each non-dimensional  
613 quantity at the peak operating point as well as the range of non-dimensional  
614 values observed between differing turbines as a percentage of the peak value.  
615 The author's note that due to water ingress into the nose cone of T1 during  
616 the experiments at KHL, no blade data was captured as such these plots are  
617 omitted from Figures 17 and 18. Furthermore, due to the timing restraints  
618 on the testing the water ingress meant it was only possible to test T1 at the  
619 0.8 and 1.0  $ms^{-1}$ . Since this time the cause of the leak has been detected  
620 and rectified.



Table 8: Table providing an overview of peak non-dimensional quantities observed, with standard deviations for a given turbine presented as well as the range of non-dimensional values recorded across the three turbines.

<b>Qty</b>	<b>Turbine 1</b>	<b>Turbine 2</b>	<b>Turbine 3</b>
Max $C_P$	0.47	0.48	0.48
U @ Max $C_P$	$1.0 \text{ m s}^{-1}$	$0.8 \text{ m s}^{-1}$	$1.0 \text{ m s}^{-1}$
$\lambda$ @ Max $C_P$	4	4	4
Max $\sigma_{C_P}$ @ $\lambda = 4$	0.013	0.015	0.013
Range $C_P$ @ $\lambda = 4$ % of Max $C_P$	6.7 %		
Max $C_\theta$	0.16	0.17	0.16
U @ Max $C_\theta$	$1.0 \text{ m s}^{-1}$	$1.0 \text{ m s}^{-1}$	$1.2 \text{ m s}^{-1}$
$\lambda$ @ Max $C_\theta$	2.5	2.5	2.5
Max $\sigma_{C_\theta}$ @ $\lambda = 2.5$	0.003	0.003	0.003
Range $C_\theta$ @ $\lambda = 2.5$ % of Max $C_\theta$	4.2 %		
Max $C_T$	1.05	1.09	1.09
U @ Max $C_T$	$0.8 \text{ m s}^{-1}$	$0.8 \text{ m s}^{-1}$	$0.8 \text{ m s}^{-1}$
$\lambda$ @ Max $C_T$	5	6.5	6.5
Max $\sigma_{C_T}$ @ $\lambda = 6.5$	0.05	0.02	0.02
Range $C_\theta$ @ $\lambda = 2.5$ % of Max $C_T$	6.8 %		

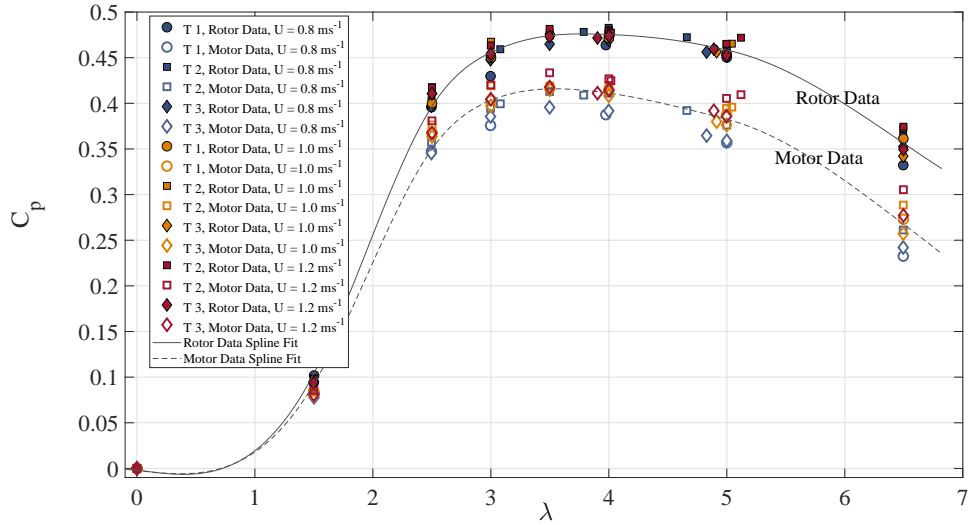


Figure 14: Characteristic power curves obtained whilst testing at KHL for each of the three turbines, the figures show both the power curves obtained considering rotor transducer measurements and motor power measurements.

621 In all cases the non-dimensional characteristics display a very good level  
 622 of repeatability, not only for each turbine at the separate velocities, but  
 623 also when comparing each of the differing turbines manufactured. With  
 624 reference to Figure 14, the largest spread of  $C_P$  values recorded was found  
 625 at the highest  $\lambda$ -value tested, namely  $\lambda = 6.5$ . This spread was found to be  
 626 larger in the  $C_P$  values derived from the motor data rather than the rotor  
 627 transducer. This would suggest, as asserted above, that motor control actions  
 628 (including winding current measurement noise) generally yield more variable  
 629 power measurements than the rotor transducer for low turbulence operation.  
 630 Drive shaft losses, taken as the difference between the motor data derived  
 631  $C_P$  and the rotor transducer derived  $C_P$ , were found to increase with  $\lambda$  and  
 632 ranged from 11% in the peak power region up to 21% at free-wheeling. The

633 losses for all three turbines were consistent, however it was found that slightly  
 634 higher losses were found for the  $0.8 \text{ ms}^{-1}$  carriage speed case. Due to these  
 635 losses, the nature of the  $C_P$  curves developed vary between those measured  
 636 via the motor data and the rotor transducer. Peak  $C_P$  derived via the motor  
 637 data was found to arise at  $3 < \lambda < 4$ . Whereas the peak power in the rotor  
 638 transducer data arose at  $\lambda = 4$ . This distortion of the power curves can be  
 639 expected as the losses found were not consistent across operating points with  
 640 aforementioned dependence on rotational velocity.

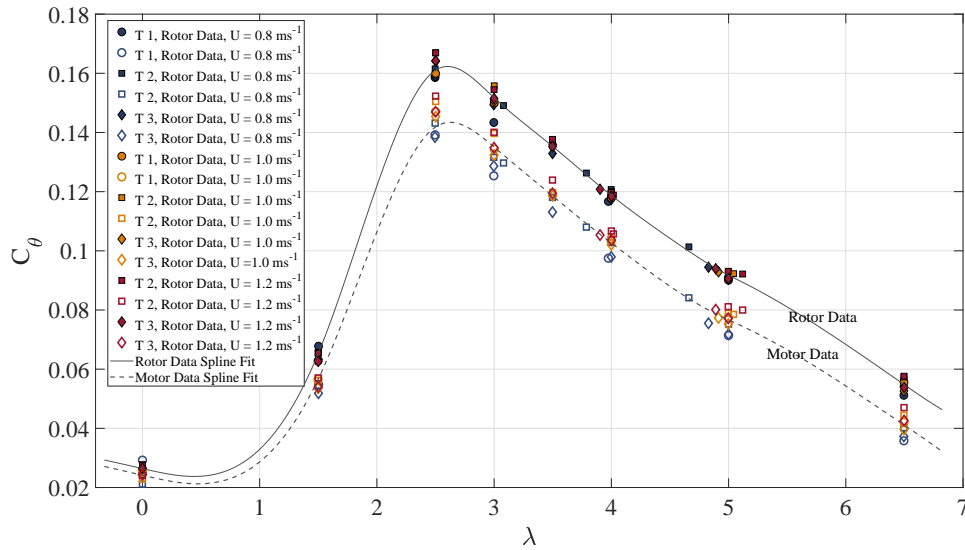


Figure 15: Characteristic torque curves obtained whilst testing at KHL for each of the three turbines, the figures show both the power curves obtained considering rotor transducer measurements and motor power measurements.

641 The non-dimensional torque coefficients observed for the KHL test cases  
 642 again show good agreement over both differing fluid velocities and for dif-  
 643 fering turbines, Figure 15. A peak rotor based  $C_\theta$  value of 0.16 was found  
 644 at  $\lambda = 2.5$ , which coincides with the findings from the other test facilities

645 discussed in Section 5.4.1. Again, the  $C_\theta$  values calculated via motor current  
 646 measurements a more widely spread than the rotor transducer based values.  
 647 Likewise, the motor data based values for the  $0.8 \text{ ms}^{-1}$  case were generally  
 648 found to be slightly lower than the other fluid velocity cases. Increased data  
 649 spread can be observed in the peak torque region as well as the at high  
 650  $\lambda$ -values.

651 Figure 16 shows very good agreement for the non-dimensional thrust co-  
 652 efficients observed across all test cases. Minimal scatter is observed until a  
 653  $\lambda$  value of 6.5, where a maximum  $C_T$  of 1.09 was observed. Given the afore-  
 654 mentioned sensitivity of the thrust loading experience to blade pitch angle  
 655 setting, this would suggest high repeatability in blade pitch angle setting.

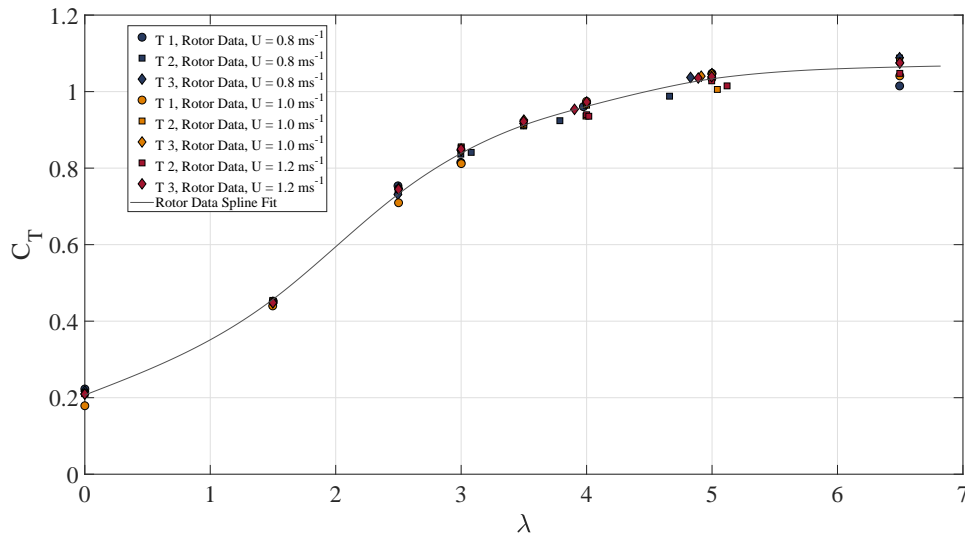


Figure 16: Characteristic thrust curves obtained whilst testing at KHL for each of the three turbines

656 The individual blade axial moments shown in Figure 17, show an excellent  
 657 grouping with each turbine comparable to the other turbines. Figure 18

658 shows the  $M_z$  moment operating in the rotational direction. There is clearly  
659 a wide spread of the data sets both between each blade for the same turbine  
660 and also for the additional and identical turbines. What can be extracted  
661 from the data sets is that they follow the same trend, as shown in Figure 15,  
662 for the torque loading over the range of  $\lambda$  values, peaking at  $\lambda \approx 2.5$  in all  
663 cases.

664 The non-dimensional parameters and blade root bending moment curves  
665 have shown that the design and manufacture of the individual turbines is of  
666 a quality that allows interchangeability and repeatability. Testing of mul-  
667 tiple turbines can be directly compared to the data sets for the individual  
668 turbines providing high levels of confidence and reliability. The introduction  
669 of turbulence, wakes, wave-current interaction, current-structural interaction  
670 or in fact any combination can be directly compared to these data sets to  
671 determine their influence of the dynamic loading of the turbines.

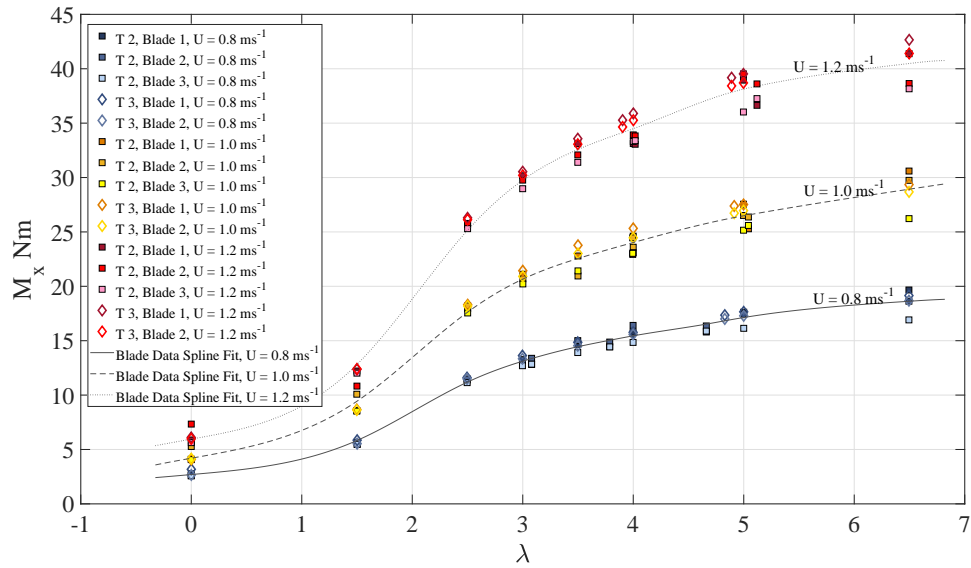


Figure 17: Characteristic blade root bending moments, flapwise or  $M_x$  moments, obtained whilst testing at KHL for each of the three turbines

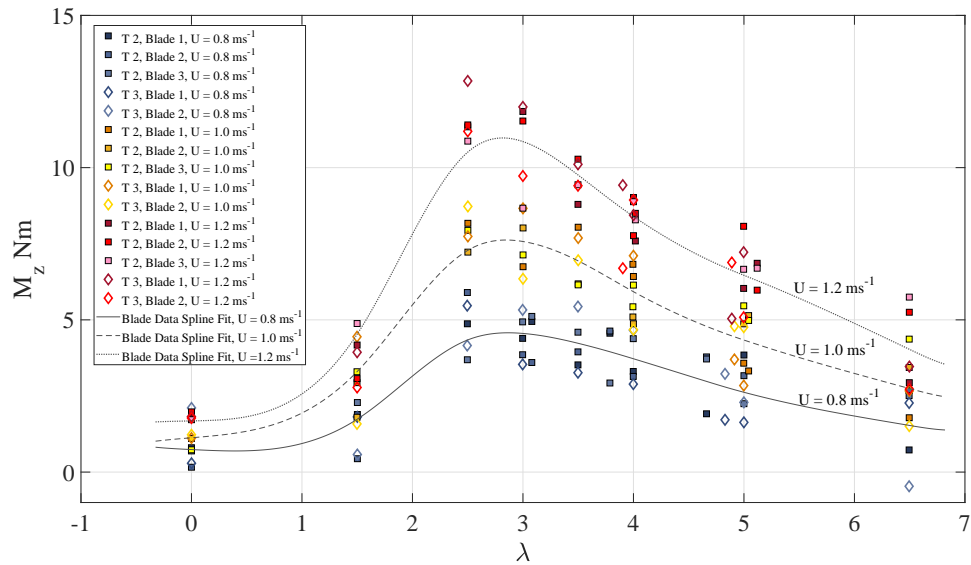


Figure 18: Characteristic blade root bending moments, edgewise or  $M_z$  moments, obtained whilst testing at KHL for each of the three turbines

672 *5.5. Discussion*

673 The results section presents the data relating to a variety of test cam-  
674 paigns for a single turbine, namely T1, followed by a comparison of the  
675 non-dimensional parameters of the three turbines manufactured to the spec-  
676 ifications detailed throughout the paper.

677 The comparison of the findings from the differing test campaigns shows  
678 that relatively repeatable results were generated. However, some significant  
679 differences were highlighted between the findings. The authors note that this  
680 was not entirely unexpected as these tests were performed at differing stages  
681 of development and design integration for the prototype turbine, turbine  
682 T1. These results, in terms of power and torque, were generated by utilising  
683 PMSM winding current measurements. The relatively large spread in the  
684 data and the deviation of the power curve recorded at IFREMER relative to  
685 the tow tank cases, suggests that detailed understanding and characterisation  
686 of motor control operations and drive shaft losses are required to generate  
687 concrete findings when using motor current data to measure rotor power  
688 and torque. Furthermore, it was considered that changes in the turbine  
689 set-up during development are likely to have changed the drive train losses  
690 characterisation - this may have impacted on the blockage correction method  
691 utilised by changing the power to thrust relationship of the turbine.

692 Another aspect of deviation between the test cases was the differing thrust  
693 characteristics observed during the testing undertaken at CNR-INM relative  
694 to the latter test cases. This was largely attributed to the differing pitch  
695 angle settings tested at CNR-INM relative to the test campaigns undertaken  
696 at IFREMER and KHL. The differing pitch angle settings were tested to

697 confirm the relative insensitivity to pitch angle variations between  $6^\circ$  and  $9^\circ$   
698 of the power produced. The inverse finding for rotor thrust was also found,  
699 as expected based on the BEMT and CFD modelling. Whilst the finding  
700 of the modelling stages seem to have been confirmed, the authors believe  
701 a structured test campaign is required to fully quantify the effects of pitch  
702 angle on power and thrust production.

703 The variability observed between facilities was of a similar magnitude  
704 which was unexpected due to the presence of approximately 2 % turbulence  
705 intensity experienced at IFREMER. This highlights the requirement for high  
706 levels of electrical shielding, a high degree of accuracy in rotor and drive  
707 train set-up and the requirement to measure rotor quantities directly. This  
708 finding is non-trivial in the quantification of dynamic loading and suggested  
709 that before undertaking more ambitious test campaigns including unsteady  
710 effects, such as testing under wave conditions and high levels of turbulence,  
711 an initial set of steady-state tests at the given facility should be undertaken  
712 as a benchmark.

713 Lastly, the mean non-dimensional quantities observed at the KHL facility  
714 for all three of the manufactured turbines showed good agreement. As such,  
715 there is a high level certainty in the turbine characterisations performed.  
716 Relatively large scatter was found for the blade root bending moment mea-  
717 surements taken. These results suggest that improved amplification and  
718 filtering of the blade root bending moment measurements maybe required,  
719 although it cannot be concluded at this stage that the differing quantities  
720 observed are spurious findings.



721 *5.6. Conclusions and Further Work*

722 The paper presents the specification of a 1/20th scale HATT design, de-  
723 tailing blade design activities as well as measurement and turbine control  
724 processes. The paper then outlines testing of the three lab scale HATTs.

725 The updated blade design yielded higher turbine performance with a rel-  
726 atively minor increase in thrust loading. A maximum  $C_P$  of 0.47 at  $\lambda = 4$   
727 was observed with a maximum  $C_T$  of 1.09 found for  $\lambda$  values above 6.5.  
728 Free-wheeling occurred at  $\lambda = 8$ , with peak torque at  $\lambda = 2.5$ .

729 The operation and design of the turbine and its instrumentation was  
730 demonstrated across the various test campaigns. Under speed control the  
731 standard deviation of the rotational velocity of the turbine was, in most cases,  
732 below 0.3 RPM, other than at free-wheeling. Under torque control torsional  
733 variations of 0.4 Nm were observed. The quantities represent variability of  
734 less than 2.5 % relative to median values and demonstrated a high degree of  
735 stability in the turbine control systems across all operating ranges.

736 Good agreement between the tests undertaken at differing facilities was  
737 found given the development and maintenance of the turbine between test  
738 campaigns. It was found that using motor current measurements to estimate  
739 turbine rotor torque and power can lead to uncertainty in results if a high  
740 degree of characterisation of motor control variability and drive shaft losses  
741 are not undertaken. Furthermore, it was found that it is not clear the effect of  
742 drive shaft losses on the blockage correction approach which will change the  
743 power to thrust characteristics for the turbine. A high degree of repeatability  
744 of the rotor quantities across all three turbines was confirmed via the test  
745 campaign undertaken at the KHL.

746 Further work is being undertaken to generate an in-depth characterisation  
747 of the three turbines tested at the KHL. This work will seek to understand in  
748 more detail the dynamic aspects associated with the turbine operation and  
749 the discrepancies between the turbines in this regard. The blade root bending  
750 moment instrumentation will be further developed with greater amplification  
751 and filtering to improve measurement consistency. Lastly, the three turbines  
752 have been tested in a variety of dynamic conditions, the findings relating  
753 to these campaigns will be presented in future. Furthermore, the turbines  
754 detailed have been utilised for array characterisation at FloWave, Edinburgh  
755 and will be used for detailed flow characterisation of two interacting turbines,  
756 with this test campaign being undertaken at IFREMER.

## 757 **Acknowledgements**

758 Funding: This work was supported by the Engineering and Physical Sci-  
759 ences Research Council [DyLoTTA –EP/N020782/1]; Horizon2020 [MARINET2-  
760 731084]; Engineering and Physical Sciences Research Council[Cardiff Univer-  
761 sity Impact Acceleration Account-EP/R51150X/1].

## 762 **References**

763 [1] Department of Energy & Climate Change, DECC Electricity Gen-  
764 eration Costs 2013 - GOV.UK, Tech. rep., Department of Energy &  
765 Climate Change, London (2013).

766 URL <https://www.gov.uk/government/publications/decc-electricity-generation-co>

767 [2] X.-P. Zhang, P. Zeng, Marine Energy Technology [Scanning

768 the Issue], Proceedings of the IEEE 101 (4) (2013) 862–865.  
769 doi:10.1109/JPROC.2013.2244735.

[3] European Parliament, Directive (EU) 2018/2001 of the European Parliament and of the Council of 11 December 2018 on the promotion of the use of energy from renewable sources, Tech. rep., European Parliament and Council of 11 December 2018, London (2018).

URL <https://eur-lex.europa.eu/legal-content/EN/ALL/?uri=uriserv:OJ.L.2018.328.0>

770 [4] C. Johnstone, D. Pratt, J. Clarke, A. Grant, A techno-economic anal-  
771 ysis of tidal energy technology, Renewable Energy 49 (2013) 101–106.  
772 doi:10.1016/J.RENENE.2012.01.054.

773 [5] IEC, IEC 61400 - Wind turbines, Tech. rep., IEC (2015).

774 URL <https://webstore.iec.ch/publication/22259>

775 [6] A. Bahaj, A. Molland, J. Chaplin, W. Batten, Power and thrust mea-  
776 surements of marine current turbines under various hydrodynamic flow  
777 conditions in a cavitation tunnel and a towing tank, Renewable Energy  
778 32 (3) (2007) 407–426. doi:10.1016/J.RENENE.2006.01.012.

779 [7] J. A. Clarke, G. Connor, A. D. Grant, C. M. Johnstone, Design and  
780 testing of a contra-rotating tidal current turbine, Proceedings of the In-  
781 stitution of Mechanical Engineers, Part A: Journal of Power and Energy  
782 221 (2) (2007) 171–179. doi:10.1243/09576509JPE296.

783 [8] T. Stallard, R. Collings, T. Feng, J. Whelan, Interactions between tidal  
784 turbine wakes: experimental study of a group of three-bladed rotors,

- 785 Philosophical Transactions of the Royal Society A: Mathematical, Phys-  
786 ical and Engineering Sciences 371 (1985) (2013) 20120159–20120159.  
787 doi:10.1098/rsta.2012.0159.
- 788 [9] P. Mycek, B. Gaurier, G. Germain, G. Pinon, E. Rivoalen, Numeri-  
789 cal and experimental study of the interaction between two marine cur-  
790 rent turbines, *International Journal of Marine Energy* 1 (2013) 70–83.  
791 doi:10.1016/j.ijome.2013.05.007.
- 792 [10] P. Mycek, B. Gaurier, G. Germain, G. Pinon, E. Rivoalen, Experimental  
793 study of the turbulence intensity effects on marine current turbines be-  
794 haviour. Part II: Two interacting turbines, *Renewable Energy* 68 (2014)  
795 876–892. doi:10.1016/J.RENENE.2013.12.048.
- 796 [11] P. Mycek, B. Gaurier, G. Germain, G. Pinon, E. Rivoalen, Experimen-  
797 tal study of the turbulence intensity effects on marine current turbines  
798 behaviour. Part I: One single turbine, *Renewable Energy* 66 (2014) 729–  
799 746. doi:10.1016/J.RENENE.2013.12.036.
- 800 [12] G. S. Payne, T. Stallard, R. Martinez, Design and manufacture of a bed  
801 supported tidal turbine model for blade and shaft load measurement  
802 in turbulent flow and waves, *Renewable Energy* 107 (2017) 312–326.  
803 doi:10.1016/J.RENENE.2017.01.068.
- 804 [13] A. Mason-Jones, Performance assessment of a Horizontal Axis Tidal  
805 Turbine in a high velocity shear environment., Ph.D. thesis, Cardiff  
806 University (2010).

- 807 [14] M. J. Allmark, Condition monitoring and fault diagnosis of tidal stream  
808 turbines subjected to rotor imbalance faults, Ph.D. thesis, Cardiff Uni-  
809 versity (2016).
- 810 [15] C. Frost, C. E. Morris, A. Mason-Jones, D. M. O’Doherty,  
811 T. O’Doherty, The effect of tidal flow directionality on tidal tur-  
812 bine performance characteristics, *Renewable Energy* 78 (2015) 609–620.  
813 doi:10.1016/j.renene.2015.01.053.
- 814 [16] C. Morris, Influence of solidity on the performance, swirl characteristics,  
815 wake recovery and blade deflection of a horizontal axis tidal turbine,  
816 Ph.D. thesis, Cardiff University (2014).
- 817 [17] M. Allmark, R. Grosvenor, P. Prickett, An approach to the characteri-  
818 sation of the performance of a tidal stream turbine, *Renewable Energy*  
819 111 (2017) 849–860. doi:10.1016/j.renene.2017.05.010.  
820 URL <http://linkinghub.elsevier.com/retrieve/pii/S0960148117303956>
- 821 [18] S. Ordonez-Sanchez, R. Ellis, K. Porter, M. Allmark, T. O’Doherty,  
822 A. Mason-Jones, C. Johnstone, Numerical models to pre-  
823 dict the performance of tidal stream turbines working under  
824 off-design conditions, *Ocean Engineering* 181 (2019) 198–211.  
825 doi:10.1016/J.OCEANENG.2019.04.027.  
826 URL <https://www.sciencedirect.com/science/article/pii/S0029801818312848>
- 827 [19] S. Ordonez Sanchez, K. Porter, C. Frost, M. Allmark, C. Johnstone,  
828 T. O’Doherty, Effects of extreme wave-current interactions on the per-

- 829 performance of tidal stream turbines, in: 3rd Asian Wave and Tidal Energy  
830 Conferenece, Singapore, 2016.
- 831 [20] A. Mason-Jones, D. O’Doherty, C. Morris, T. O’Doherty, C. Byrne,  
832 P. Prickett, R. Grosvenor, I. Owen, S. Tedds, R. Poole, Non-dimensional  
833 scaling of tidal stream turbines, *Energy* 44 (1) (2012) 820–829.  
834 doi:10.1016/J.ENERGY.2012.05.010.
- 835 [21] D. Egarr, T. O’doherly, S. Morris, R. Ayre, Feasibility study using com-  
836 putational fluid dynamics for the use of a turbine for extracting energy  
837 from the tide, in: 15th Australasian Fluid Mechanics Conference, 2004.  
838 doi:10.13140/2.1.4852.3041.
- 839 [22] T. Nevalainen, C. Johnstone, A. Grant, A sensitivity analysis on tidal  
840 stream turbine loads caused by operational, geometric design and inflow  
841 parameters, *International Journal of Marine Energy* 16 (2016) 51–64.  
842 doi:10.1016/J.IJOME.2016.05.005.
- 843 [23] R. Ellis, M. Allmark, T. O’Doherty, A. Mason-Jones, S. Ordonez-  
844 Sanchez, K. Johannesen, C. Johnstone, Design process for a scale hor-  
845 izontal axis tidal turbine blade, in: 4th Asian Wave and Tidal Energy  
846 Conference, Taipei, 2018.
- 847 [24] F. R. Menter, A comparison of some recent eddy-viscosity turbulence  
848 models, *Journal of Fluids Engineering, Transactions of the ASME*  
849 118 (3) (1996) 514–519. doi:10.1115/1.2817788.
- 850 [25] S. A. El-Shahat, G. Li, F. Lai, L. Fu, Investigation of parame-  
851 ters affecting horizontal axis tidal current turbines modeling by blade

- 852 element momentum theory, *Ocean Engineering* 202 (2020) 107176.  
853 doi:10.1016/j.oceaneng.2020.107176.
- 854 [26] S. Ordonez-Sanchez, M. Allmark, K. Porter, R. Ellis, C. Lloyd, I. Santic,  
855 T. O’Doherty, C. Johnstone, Analysis of a Horizontal-Axis Tidal Turbine  
856 Performance in the Presence of Regular and Irregular Waves Using Two  
857 Control Strategies, *Energies* 12 (3) (2019) 367. doi:10.3390/en12030367.  
858 URL <http://www.mdpi.com/1996-1073/12/3/367>
- 859 [27] B. Gaurier, G. Germain, J. Facq, C. Johnstone, A. Grant, A. Day,  
860 E. Nixon, F. Di Felice, M. Costanzo, Tidal energy “Round Robin”  
861 tests comparisons between towing tank and circulating tank re-  
862 sults, *International Journal of Marine Energy* 12 (2015) 87–109.  
863 doi:10.1016/J.IJOME.2015.05.005.  
864 URL <https://www.sciencedirect.com/science/article/pii/S2214166915000223>
- 865 [28] BS 8422:2003 - Force measurement. Strain gauge load cell systems.  
866 Calibration method, Tech. rep., BSI (2003). doi:0 580 42746 3.  
867 URL <https://shop.bsigroup.com/ProductDetail/?pid=000000000030067617>

## 868 **Appendix A. Consideration of Reynolds Effects**

869 To confirm the comparisons made in Sections 5.4.1 and 5.4.2 were not sub-  
870 ject to Reynolds effects, a comparison of non-dimensional quantities for tests  
871 undertaken at differing flow speeds and associated chord based Reynold’s  
872 numbers undertaken at IFREMER were considered. Figure A.19 shows  
873 the non-dimensional power coefficient distribution for differing chord based  
874 Reynolds numbers. Here the chord based Reynolds number is defined as:

$$RE_{0.7Chord} = \frac{\rho \cdot C_{0.7} \cdot U}{\mu} \quad (\text{A.1})$$

875 where,  $\rho$  is the fluid density in  $kgm^{-3}$ ,  $C_{0.7}$  is the chord length at 70 % of  
 876 the radius in  $m$ ,  $U$  is the mean fluid velocity in  $ms^{-1}$  and  $\mu$  is the dynamic  
 877 viscosity in  $Pa \cdot s$ . Figure A.19 shows that Reynolds effects become negligible,  
 878 with a variation of 1 %, for Reynold's numbers above  $RE_{0.7Chord} = 6.48E+4$ .

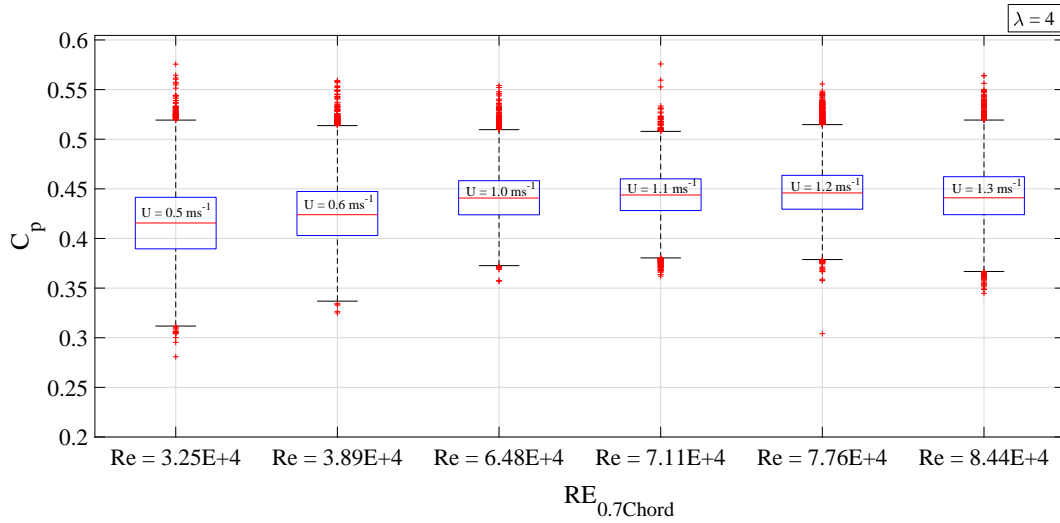


Figure A.19: Comparison of  $C_P$  values observed for tests under taken at differing fluid velocities. The  $C_P$  values are plotted against chord length based Reynold's Number for a fixed  $\lambda$ -value of  $\lambda = 4$ .

## 879 Appendix B. Instrumentation Calibration

### 880 Appendix B.0.1. Rotor Thrust and Torque Transducer Calibrations

881 The rotor thrust and torque transducers were calibrated by applied mea-  
 882 surements. Calibration certificates were provided with the transducers de-



883 tailing the calibrations undertaken and reporting on non-linearity, hysteresis  
 884 and cross-axis sensitivity.

Table B.9: Summary of calibration results for the 3 torque thrust transducers as undertaken by Applied Measurements Ltd.

<b>Qnty</b>	<b>Turbine 1</b>	<b>Turbine 2</b>	<b>Turbine 3</b>
Serial No.	54283	54284	157961
Thrust Gradient, A/N	5.308E-3	5.349E-3	5.333E-3
Thrust non-linearity	$\pm 0.043\%$ FS	$\pm 0.056\%$ FS	$\pm 0.043\%$ FS
Thrust hysteresis	$< 0.074\%$ FS	$< 0.098\%$ FS	$< 0.074\%$ FS
Thrust cross-sensitivity	$< 0.23\%$ FS	$< 0.45\%$ FS	$< 0.23\%$ FS
Torque Gradient, A/Nm	8.00E-2	8.01E-2	8.00E-2
Torque non-linearity	$\pm 0.031\%$ FS	$\pm 0.031\%$ FS	$\pm 0.031\%$ FS
Torque hysteresis	$< 0.075\%$ FS	$< 0.062\%$ FS	$< 0.075\%$ FS
Torque cross-sensitivity	$< 0.35\%$ FS	$< 0.18\%$ FS	$< 0.35\%$ FS

885 *Appendix B.0.2. Flap-Wise Blade Root Bending Moment Calibrations*

886 The three flap-wise blade root bending moment transducers for each tur-  
 887 bine were calibrated according to the BSI - standard [28]. Increasing moments  
 888 were applied to the transducers and the current output from the amplifiers  
 889 were recorded in Amps. The weights used to create the moments had an  
 890 uncertainty of 0.001g with the distance over which the load was applied had  
 891 an uncertainty of 0.1 mm. Figures B.20 and B.21 show the calibration and  
 892 residuals associated with the linear fit for hub 1, blade 2. Tables B.10 to B.12  
 893 show the gradients and uncertainties for each of the calibrated transducers.

Table B.10: Summary of calibration results for flap-wise blade root bending moment transducers, Turbine 1.

<b>Qty</b>	<b>Blade 1</b>	<b>Blade 2</b>	<b>Blade 3</b>
Gradient A/Nm	1.59E-4	1.62E-4	1.57E-4
Fit Uncertainty (SEE), Nm	0.62	0.45	0.44
Bias Uncertainty, Nm	0.12	0.12	0.12
Total Uncertainty, Nm	0.63	0.47	0.46

Table B.11: Summary of calibration results for flap-wise blade root bending moment transducers, Turbine 2.

<b>Qty</b>	<b>Blade 1</b>	<b>Blade 2</b>	<b>Blade 3</b>
Gradient A/Nm	1.60E-4	1.63E-4	1.62E-4
Fit Uncertainty (SEE), Nm	0.43	0.41	0.90
Bias Uncertainty, Nm	0.12	0.12	0.12
Total Uncertainty, Nm	0.45	0.43	0.90

Table B.12: Summary of calibration results for flap-wise blade root bending moment transducers, Turbine 3.

<b>Qty</b>	<b>Blade 1</b>	<b>Blade 2</b>	<b>Blade 3</b>
Gradient A/Nm	1.60E-4	1.62E-4	NA
Fit Uncertainty (SEE), Nm	0.41	0.42	NA
Bias Uncertainty, Nm	0.12	0.12	NA
Total Uncertainty, Nm	0.43	0.44	NA

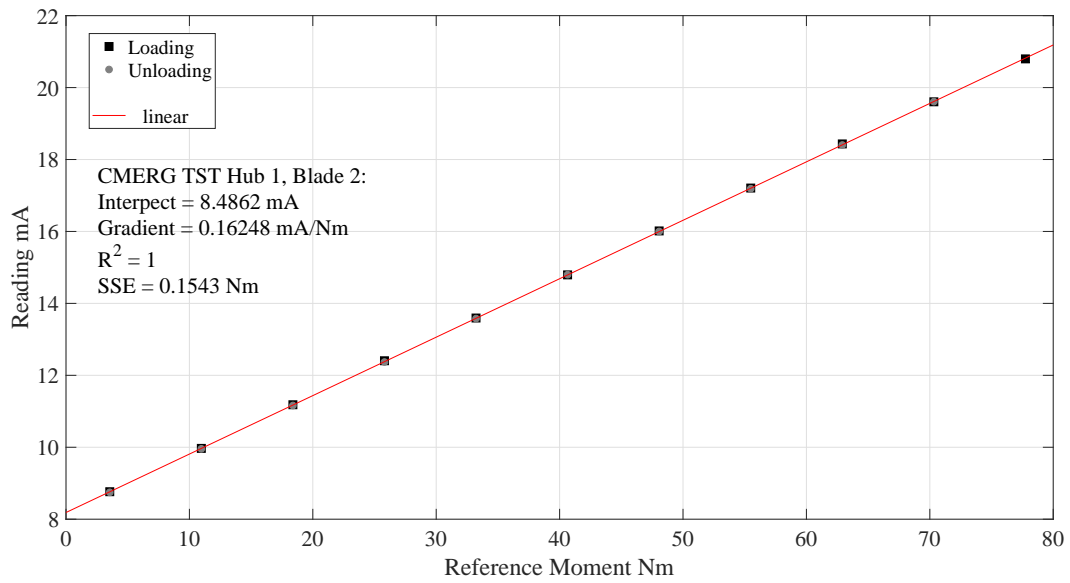


Figure B.20: The calibration results for the flapwise blade root bending moment transducer for blade 2, hub 1.

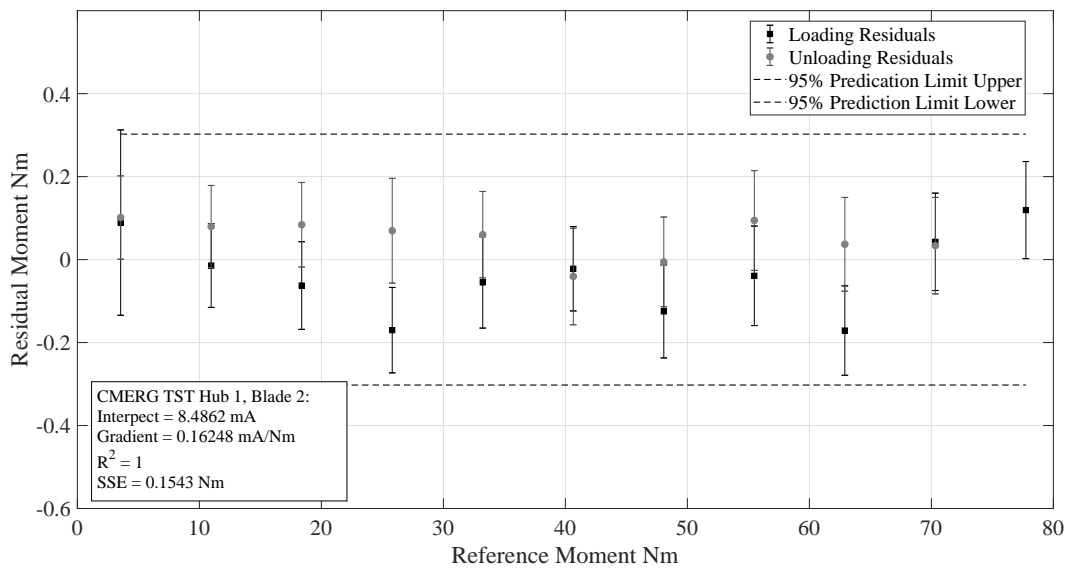


Figure B.21: Fitted residuals for calibration results for the flapwise blade root bending moment transducer for blade 2, hub 1.

894 *Appendix B.0.3. Edge-Wise Blade Root Bending Moment Calibrations*

895 The edge-wise blade root bending moment calibrations were undertaken  
896 in-situ comparing the outputs from the blade root bending moment trans-  
897 ducers with the outputs from the calibrated rotor torque transducer. In this  
898 way the relationship in Equation B.1 was assumed to hold for mean quanti-  
899 ties. Furthermore, it was assumed that the mean edge-wise bending moment  
900 from each blade was equal for a given test. This method gave relatively good  
901 results, however large uncertainties were found and can be seen in the spread  
902 of data in Figure 18. Improved calibrations for this measurement are being  
903 undertaken for subsequent test campaigns.

$$\bar{\tau}_{rotor} = \sum_{i=1}^3 M_{zi} \quad (\text{B.1})$$